




Quantitative Analysis of Seismicity in Iran

MOHAMMAD RAEESI,¹  ZOYA ZARIFI,² FARAMARZ NILFOUROUSHAN,^{3,4} SAMAR AMINI BOROUJENI,⁵ and KRISTY TIAMPO⁶

Abstract—We use historical and recent major earthquakes and GPS geodetic data to compute seismic strain rate, geodetic slip deficit, static stress drop, the parameters of the magnitude–frequency distribution and geodetic strain rate in the Iranian Plateau to identify seismically mature fault segments and regions. Our analysis suggests that 11 fault segments are in the mature stage of the earthquake cycle, with the possibility of generating major earthquakes. These faults primarily are located in the north and the east of Iran. Four seismically mature regions in southern Iran with the potential for damaging strong earthquakes are also identified. We also delineate four additional fault segments in Iran that can generate major earthquakes without robust clues to their maturity. The most important fault segment in this study is the strike-slip system near the capital city of Tehran, with the potential to cause more than one million fatalities.

Key words: Geodetic strain rate, seismic strain rate, stress drop, Gutenberg-Richter parameters, major historical and recent seismicity in the Iranian Plateau.

1. Introduction

The present tectonics of Iran result from the convergence of the Arabian and the Eurasian plates in the form of continental collision (Falcon 1974; Berberian and King 1981), with the exception of the Makran subduction zone to the southeast, where a remnant part of the Tethys oceanic lithosphere subducts northward beneath southeast Iran (Nilforoushan

et al. 2003; Zarifi et al. 2014). Within Iran, most of the deformation is accommodated in major fold and thrust belts such as Zagros, Alborz and Kopeh Dagh and along large strike-slip fault systems, which tectonically define different blocks such as the Central Iran and Lut (Masson et al. 2005) (Fig. 1). A signature of this complex tectonic setting is the high rate of seismicity in the Iranian plate. Although incomplete, the USGS database records more than 30 documented earthquakes of $M > 7.0$ in Iran during recent history.

A number of researchers have assessed the seismic hazard in Iran and assigned different seismic zonation (e.g., Nowroozi and Ahmadi 1986; Ahmadi et al. 1989; Mirzaei et al. 1997, 1999; Tavakoli and Ghafory Ashtiany 1999). Tavakoli and Ghafory Ashtiany (1999) divided the Iranian Plate into 20 seismotectonic provinces with the largest earthquakes (7.9 ± 0.4) in the Kopeh Dagh, Alborz, and Van area in Turkey. Mirzaei et al. (1997) considered five seismotectonic provinces for Iran where those zones with the largest estimated earthquakes include the areas presented in Tavakoli and Ghafory Ashtiany (1999). The association of destructive earthquakes in modern and historical times with populated areas presents a grim view on the number of future fatalities due to earthquakes in Iran. Bilham (2009) classified Iran among the six most hazardous countries worldwide, which have hosted both the most fatal earthquakes and the greatest number of events in the last 500 years.

Quantitative analysis of seismicity in Iran can advance our understanding of seismic hazard potential in this country. In this study, we use the available earthquake data from 1900 to 2016 to evaluate the seismic strain rate. Using geodetic data (1999–2013), we also evaluate the geodetic shear strain rate. Using regional seismicity from the Iranian Seismological

¹ Bergen, Norway. E-mail: mrae097@gmail.com

² Department of Earth Sciences, University of Western Ontario, London, ON, Canada.

³ Department of Industrial Development, IT and Land Management, University of Gävle, Gävle, Sweden.

⁴ Lantmäteriet, Gävle, Sweden.

⁵ Department of Earth Sciences, Uppsala University, Uppsala, Sweden.

⁶ CIRES and Department of Geological Sciences, University of Colorado at Boulder, Boulder, CO, USA.

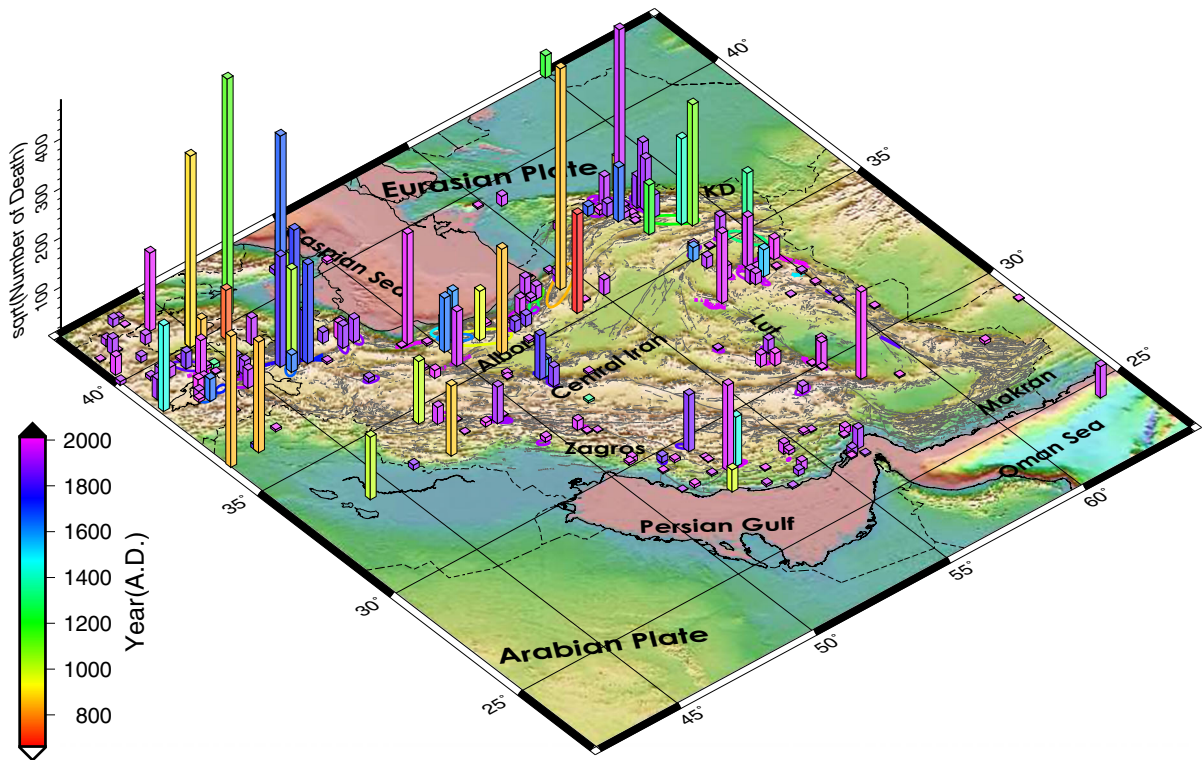


Figure 1

The known damaging earthquakes in the Iranian Plateau. The bars are colored based on date of the earthquake and the height of the bars show square root of the number of deaths (Ambraseys and Melville 1982; National Geophysical Data Center, NOAA 2016). The known surface ruptures and macroseismic areas are colored based on the date of the causative earthquake. KD in northeast of Iran stands for Kopeh Dagh ranges

Center (IRSC) since 1996, we compute variations in the Gutenberg–Richter (G–R) parameters (Gutenberg and Richter 1944), a - and b -value, around major fault systems in Iran and relate the variations to the maturity of the seismic cycle for a number of fault systems. We use the integrated results and the approximate location of the historical devastating earthquakes (before 1900) to delineate some areas which have a high potential of seismic hazard.

Two sets of numbering are used in this work. The first set refers to numbering of the macroseismic areas and earthquakes that are listed in Table 1 and are shown in Figs. 2 and 3. For simplicity, we cite earthquakes as 1997/05/10 (7.3, 170). The numbers in parenthesis refer to the magnitude and the numbering of earthquakes, respectively. The second set of numbers refers to numbering of zones used in computation of the G–R parameters as given in Table 2 and Figs. 10, 11 and 12.

2. Major Seismicity in the Iranian Plateau

The oldest documented major earthquake in the Iranian Plateau and its surroundings dates back to the second millennium BC. Based on macroseismic data from historical sources, field studies and instrumental data, more than 50 earthquakes with $M \geq 7$ are assigned to the Iranian Plateau (Ambraseys and Melville 1982; National Geophysical Data Center, NOAA 2016). These major earthquakes, along with additional large and moderate earthquakes, have caused more than 1,936,000 fatalities (Fig. 1). Major earthquakes in Iran primarily are associated with the Iranian Crescent, a zone that extends from northwest Iran, through north (Alborz), to the northeast (Kopeh Dagh) and then with a southward turn it covers the limits of the Lut Block (Ambraseys 1977).

Major historical earthquakes of 1042 (7.6, 28), 1721 (7.7, 63), 1780 (7.7, 68), and 1840 (7.4, 74) are

Table 1

Earthquakes in the Iranian Plateau with known macroseismic area (Ambraseys and Melville 1982), surface rupture, or more than 100 deaths (Ambraseys and Melville 1982; National Geophysical Data Center, NOAA 2016)

Date	Region	Lon.	Lat.	Mag.	Dead	Code
-2000	Ashkhabat	58.20	38.00	7.1		1
-0400	Rey	51.80	35.50	7.6		2
0010	Nisa	58.30	38.00	7.1		3
0662/04/26	Qumis	54.00	35.30		40,000	4
0735	Vayots-Dzor	45.60	39.70	6.5	10,000	5
0743	Eivan-Kay	52.20	35.30	7.2		6
0763	Khurasan	59.30	33.30	7.6		7
0805/12/02	Sistan	60.50	29.50	7.0		8
0815	Sistan	60.50	29.50	7.0		9
0819/06	Balkh	65.40	36.40	7.4		10
0845/09/06	Mawsil	43.10	36.20		50,000	11
0847	Mawsil	42.08	36.21		70,000	12
0850/07/15	Ray	51.20	35.30		45,000	13
0851	Dvin	44.60	40.00	5.2	12,000	14
0854	Tovin	45.00	40.00		2000	15
0855	Ray	51.50	35.60	7.0		16
0856/12/22	Qumis	54.30	36.20	7.9	200,000	17
0858/01	Dvina	44.60	40.00	5.2	12,000	18
0871/11/18	Saimareh	47.20	33.20	6.8	20,000	19
0893/12/28	Dvin	44.60	40.00	6.0	150,000	20
0943/08/20	Nisa	58.30	38.00		5000	21
0953/08/20	Nisa	58.30	38.00	7.1		22
0958/02/23	Taleghan	51.10	36.00	7.7	10,000	23
0978/06/17	Taheri	52.30	27.70	5.3	2000	24
1007/09/17	Dinavar	44.20	33.20		16,000	25
1008/04/27	Dinavar	47.40	34.60	7.0	16,000	26
1042/08/21	Tabriz	46.20	38.00		40,000	27
1042/11/04	Tabriz	46.30	38.10	7.6	50,000	28
1052/06/02	Baihaq	57.70	36.20	7.0		29
1101	Khorasan	59.00	36.00	6.5	60,000	30
1127	Firrim	53.60	36.30	6.8		31
1139	Gyzndzha	46.30	40.30		230,000	32
1177/05	E Buyin-Zara	50.70	35.70	7.2		33
1208	Gurgandzhe	60.00	42.00	6.1	2000	34
1209	Nishapur	57.80	36.40	7.6	10,000	35
1270/10/07	Nishapur	58.80	36.20	7.1	10,000	36
1272/07/29	Tabriz	46.20	38.00		250	37
1301	Firrim	53.20	36.10	6.7		38
1319	Ararat	44.50	39.10		75	39
1336/10/21	Khaf	59.70	34.70	7.6	20,000	40
1389/02	Nishapur	58.80	36.20	7.6		41
1405/11/23	Nishapur	58.80	36.20	7.6	30,000	42
1440	Qir	53.10	28.40	7.1	10,000	43
1444	Nemrutmtns	42.20	38.70		30,000	44
1483/02/18	Makran	57.90	24.90	7.7		45
1485/08/15	Pul-Rud	50.50	36.70	7.2	1000	46
1549/01/30	Qayen	59.10	33.50		3000	47
1574	Fin	51.40	34.00		1200	48
1608/04/20	Taleghan	50.50	36.40	7.6	10,000	49
1618/12/19	Dughabad	58.00	35.00		800	50
1639/05/04	Qazvin	50.00	36.20		12,000	51
1641/02/05	Dehkhareghan	46.10	37.90	6.8	1200	52
1648/03/31	Van	43.50	38.30	6.5	2000	53
1664	Tabriz	46.30	38.10		1500	54

Table 1
continued

Date	Region	Lon.	Lat.	Mag.	Dead	Code
1667/11	Shemakha	48.60	40.60	6.9	80,000	55
1667/11/18	Shirvan	57.50	37.20		12,000	56
1669/01/04	Shemakha	48.60	40.60	5.7	7000	57
1673/07/30	Mashhad	59.30	36.30	6.6	5600	58
1679/06/04	Dvina	44.70	40.10	5.9	7600	59
1695/05/11	Isfarain	57.00	37.80	7.0	360	60
1696/04/14	Chaldran	43.90	39.10	7.0		61
1715/03/08	Van	43.90	38.40	6.6		62
1721/04/26	Tabriz	46.70	37.90	7.7	40,000	63
1727/11/18	Tabriz	46.30	38.00		77,000	64
1755/06/07	Kashan	51.50	34.00		1200	65
1778/12/15	Kashan	51.30	34.00	6.2	8000	66
1779/12/27	Tabriz	46.70	38.00	6.5	10,000	67
1780/01/08	Tabriz	46.00	38.20	7.7	50,000	68
1824/06/02	Shahpur	51.60	29.70		150	69
1824/06/25	Shiraz	52.40	29.80	6.4		70
1830/03/27	Damavand	52.50	35.70		500	71
1830/05/09	Damavand	52.10	35.70		500	72
1838	Nusratabad	59.90	29.60	7.0		73
1840/07/02	Ararat	43.90	39.50	7.4	1049	74
1843/04/18	Khoy	44.90	38.70	5.9	1000	75
1844/05/12	Kashan	51.40	33.60	6.4	1500	76
1844/05/13	Miyaneh	48.00	37.40	6.9		77
1851/06	Quchan	58.40	36.80	6.9	2000	78
1852/02/22	Quchan	58.40	37.10	5.8	2000	79
1853/05/05	Shiraz	52.50	29.60	6.2	13,000	80
1863/12/30	Ardabil	47.60	38.22	6.1	500	81
1864/01/03	Lenkoran	48.28	38.25		500	82
1864/12/07	Zurbatiyah	45.98	33.38	6.4	100	83
1871/12/23	Quchan	58.40	37.40	7.2	2000	84
1872/01/06	Quchan	58.30	37.30	6.3	4000	85
1879/03/22	Garmarud	47.90	37.80	6.7	2000	86
1879/04/02	Bojnurd	57.40	37.50	6.7	700	87
1880/07/04	Garrus	47.50	36.50	5.6	60	88
1880/08	Bastak	54.20	27.10		120	89
1884/05/19	Qeshm	55.91	26.81		238	90
1890/07/11	Shahrud	54.60	36.60	7.2	171	91
1893/11/17	Quchan	58.40	37.20	7.1	18,000	92
1895/01/17	Quchan	58.40	37.10	6.8	11,000	93
1895/07/08	Uzun-Ada	53.70	39.50	7.4		94
1896/01/02	Sangabad	48.30	37.80		300	95
1896/01/04	Khalkhal	48.30	37.80	6.7	2200	96
1896/01/05	Khoy	45.00	38.50		800	97
1897/01/11	Qeshm	56.26	26.95	6.4	1600	98
1899/12/31	Turkey	43.50	41.60	5.6	247	99
1900/02/24	Khoy	44.87	38.45	5.4		100
1900/07/12	Kars	43.10	40.30	5.9	140	101
1903/04/19	Turkey	42.40	39.10		1700	102
1903/04/28	Malazgirt	42.50	39.10	6.3	3560	103
1903/05/28	Varginis	42.70	40.90	5.8	1000	104
1903/09/25	Kashmar	58.20	35.20	6.5	350	105
1905/10/21	Caucasus	42.00	42.00	7.5		106
1909/01/23	Silakhur	49.13	33.41	7.4	5500	107
1911/04/18	Ravar	57.03	31.23	6.7	700	108
1923/05/25	Turbat	59.20	35.20	5.7	2200	109

Table 1
continued

Date	Region	Lon.	Lat.	Mag.	Dead	Code
1923/09/17	Bojnurd	57.70	37.20	6.4	157	110
1923/09/22	Laleh	56.63	29.51	6.9	200	111
1925/01/09	Ardahan	42.80	41.20	5.8	200	112
1925/12/14	Bajestan	58.10	34.60	5.5	500	113
1926/10/22	Armenia	43.70	40.70	5.7	360	114
1929/05/01	Kopet-Dagh	57.60	37.80	7.3	3800	115
1929/05/13	Quchan	57.50	38.12			116
1929/07/13	Faruj	58.00	37.50	5.8	5	117
1929/07/15	Khuzestan	49.70	32.20	6.2	6	118
1930/05/06	Salmas	44.70	38.10	7.2	1360	119
1930/10/02	Damavand	51.99	35.76	5.2		120
1931/04/27	Zangezur	46.00	39.20	6.3	2890	121
1932/05/20	Turbat	53.40	36.60	5.6	1070	122
1933/11/28	Bahabad	56.00	32.10	6.3	4	123
1935/03/05	Alborz	53.30	36.30	6.0	60	124
1935/04/11	Kusut	53.50	36.30	6.3	690	125
1936/06/30	Abiz	60.00	33.00	6.2	12	126
1941/02/16	Mussavieh	58.60	33.50	6.3	730	127
1941/09/10	Van	43.30	39.50	6.0	430	128
1945/07/29	Van	43.30	38.50		300	129
1945/11/27	Makran	63.00	24.50	8.1	4000	130
1946/11/04	Balkanabat	55.40	39.30	7.5	400	131
1947/08/05	Gwadar	63.00	25.50	7.1		132
1947/09/23	Dustabad	58.70	33.40	6.9	500	133
1948/10/05	Ashkhabat	58.32	37.95	7.3	110,000	134
1953/02/12	Torud	55.10	35.40	6.4	970	135
1956/10/31	Bastak	54.40	27.20	6.8	347	136
1957/07/02	Band Pey	52.70	36.10	7.0	1100	137
1957/12/13	Farsinaj	47.80	34.30	7.1	1200	138
1958/08/16	Firuzabad	47.90	34.40	6.7	132	139
1960/04/24	Lar	54.50	28.00	6.0	420	140
1962/04/01	Mussavieh	59.00	33.60	5.5	5	141
1962/09/01	Buyin-Zara	49.87	35.63	7.2	12,225	142
1963/03/24	Karkhaneh	47.90	34.40	7.2	100	143
1963/03/31	Hendojan	57.90	37.00	7.0	4	144
1968/08/31	Dasht Bayaz	59.00	34.00	7.3	10,488	145
1968/09/01	Ferdows	58.20	34.00	6.5	700	146
1968/09/14	Qir	53.23	28.34	6.1		147
1970/07/30	Karnaveh	55.90	37.80	6.7	220	148
1972/04/10	Qir	52.80	28.40	6.9	30,000	149
1976/04/08	Gazli	63.77	40.31	7.0		150
1976/05/17	Gazli	63.47	40.38	7.0		151
1976/11/24	Muradiye	44.03	39.12	7.3	5000	152
1977/03/21	Bandar Abbas	56.39	27.61	6.9	167	153
1977/04/06	Naghan	50.68	31.98	5.9	366	154
1977/12/19	Gisk	56.47	30.95	5.8	584	155
1978/09/16	Tabas	57.43	33.39	7.3	20,000	156
1979/01/16	Bonzanabad	59.47	33.90	6.8	200	157
1979/11/14	Korizan	59.74	33.92	6.6	350	158
1979/11/27	Koli	59.73	33.96	7.0	17	159
1981/06/11	Golbaf	57.72	29.91	6.7	3000	160
1981/07/28	Golbaf-Sirch	57.79	30.01	7.1	3000	161
1983/10/30	Erzurum	42.19	40.33	6.9	1342	162
1984/03/19	Gazli	63.35	40.32	7.0		163
1988/12/07	Leninakan	44.19	40.99	6.8	25,000	164

Table 1

continued

Date	Region	Lon.	Lat.	Mag.	Dead	Code
1989/05/27	Do Gobadan	50.92	30.17	5.8	114	165
1990/06/20	Rudbar	49.41	36.96	7.4	50,000	166
1990/11/06	Furg	55.46	28.25	6.4	22	167
1997/02/04	Bojnurd	57.29	37.66	6.5	88	168
1997/02/28	Ardabil	48.05	38.08	6.1	1100	169
1997/05/10	Birjand	59.81	33.83	7.2	1728	170
2000/12/06	Nebitdag	54.80	39.57	7.0	11	171
2002/06/22	Ab-Garm	49.05	35.63	6.5	261	172
2003/12/26	Bam	58.31	29.00	6.6	31,000	173
2005/02/22	Zarand	56.82	30.75	6.4	612	174
2011/01/18	Garhi Khair	63.95	28.78	7.2	3	175
2011/10/23	Ercis	43.51	38.72	7.1	604	176
2012/08/11	Ahar	46.83	38.33	6.5	306	177
2013/04/16	Mashkal	62.00	28.03	7.7	40	178

The codes refer to the numbering in Fig. 2

associated with the NW-Iran zone. The North Tabriz fault ruptured in 1042. Approximately six centuries later, two overlapping earthquakes of 1721 (7.7, 63) and 1780 (7.7, 68) ruptured the North Tabriz Fault again and the rupture extended to the southeast of Tabriz. This fault system has not experienced any major earthquakes since 1780. Post-1900, major activity in the northwest Iran includes the 1905/10/21 (7.5, 106) Caucasus in Georgia, 1930/05/06 (7.2, 119) Salmas, 1976/11/24 (7.3, 152) Chalderan in Turkey, and 2011/10/23 (7.1, 176) Ercis in Turkey earthquakes. The 1976 Chalderan earthquake rupture experienced approximately 63 km of right-lateral surface rupture with an azimuth of 110° that stopped at the Turkey–Iran border, 45 km away from joining another fault system with azimuth of 145°, the 1840/07/02 (7.4, 74) Maku–Ararat earthquake. The 2011 Ercis event was a reverse earthquake, typical for the Zagros collision zone (Dogan and Karakas 2013).

Further to the east, Alborz hosts a substantial portion of the reported historical earthquakes. However, this might be due to greater reporting by the higher population of central Alborz. Earthquakes from sparsely populated areas could have remained undetected. The oldest documented event in Alborz dates back to the fourth century BC in the Ray region with an assigned magnitude of 7.6. Earthquakes of 0743 AD (7.1, 6) and 0958 (7.7, 23) are associated with the central and western Alborz. The sequence continued in the second millennium with the earthquakes of 1177

(7.2, 33), 1485 (7.2, 46) and 1608 (7.6, 49). Provided that the catalog of major historical earthquakes in Alborz is complete, which is very unlikely, the shortest quiescent period for the western Alborz is approximately 100 years. The eastern Alborz has experienced the largest historical intraplate earthquake of the Iranian Plateau in 0856 AD (7.9, 17). The post-1900 earthquakes in Alborz are limited to the 1962/09/01 (7.2, 142) along its south-western boundary and the 1990/06/20 (7.4, 166) earthquake in the western Alborz (Table 1; Fig. 2).

Similar to Alborz, the Kopeh Dag hosts substantial major historical earthquakes and the associated causative faults are aligned in the NW–SE direction. The events within Kopeh Dag are primarily strike-slip. Nevertheless, those located along its north-eastern bound have dominant thrust components. The major earthquakes of 2000 BC (7.1, 1), 0010 AD (7.1, 3), 0943 (7.6, 21), 1209 (7.6, 35), 1270 (7.1, 36), 1389 (7.6, 41), 1405 (7.6, 42), 1871 (7.2, 84), 1893 (7.1, 92), 1929/05/01 (7.3, 115), 1946/11/04 (7.5, 131), 1948/10/05 (7.3, 134), 1963/03/31 (7.0, 144) and 2000/12/06 (7.0, 171) indicate more frequent major earthquakes and consequently shorter quiescent periods compared to Alborz.

The Lut Block in the east of Iran is surrounded mainly by strike-slip fault systems. Earthquakes of 0763 (7.6, 7), 1336 (7.6, 40) and 1618 (7.6, 50) are probably associated with rims of the Lut Block. Substantial parts of the strike-slip systems

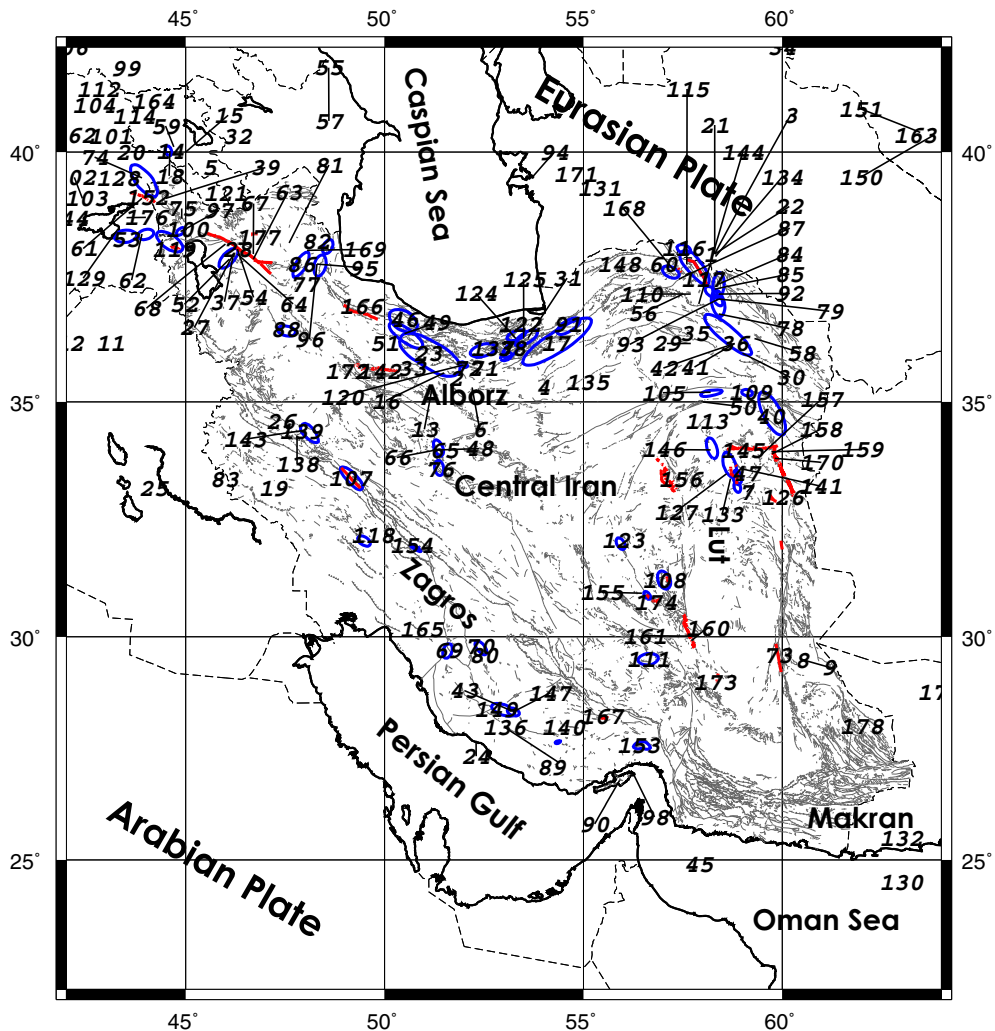


Figure 2

Earthquakes in the Iranian Plateau with known macroseismic area (blue) (Ambraseys and Melville 1982), surface rupture (red), or with a death toll of more than 100 (Ambraseys and Melville 1982; National Geophysical Data Center, NOAA 2016). See Table 1 for more information about the numbered earthquakes. The thin gray lines show the known faults in Iran

surrounding the Lut Block ruptured during the last century in the form of major earthquakes. The earthquakes of 1968/08/31 (7.3, 145), 1978/09/16 (7.3, 156), 1979/11/27 (7.0, 159), 1981/07/28 (7.2, 161), and 1997/05/10 (7.3, 170) indicate a high rate of seismicity in the last 70 years around the Lut Block (Table 1; Fig. 2).

The known historical major earthquakes in Zagros are limited to the 1008 (7.0, 26) and 1440 (7.1, 43) events. The post-1900 major earthquakes along the northeastern boundary of Zagros include the 1909/01/23 (7.4, 107) and 1957/12/13 (7.0, 138) events (Table 1; Fig. 2).

3. Analysis

We compute seismic strain rate, geodetic strain rate, stress drop and the Gutenberg–Richter parameters for the study area. In this section, the procedures employed in these analyses are explained briefly.

3.1. Seismic Strain Rate

Earthquakes are not only the result of tectonic deformation, but also contribute to it through quasi-plastic deformation. Kostrov and Das (1988) related seismic slip to seismic moment by considering an

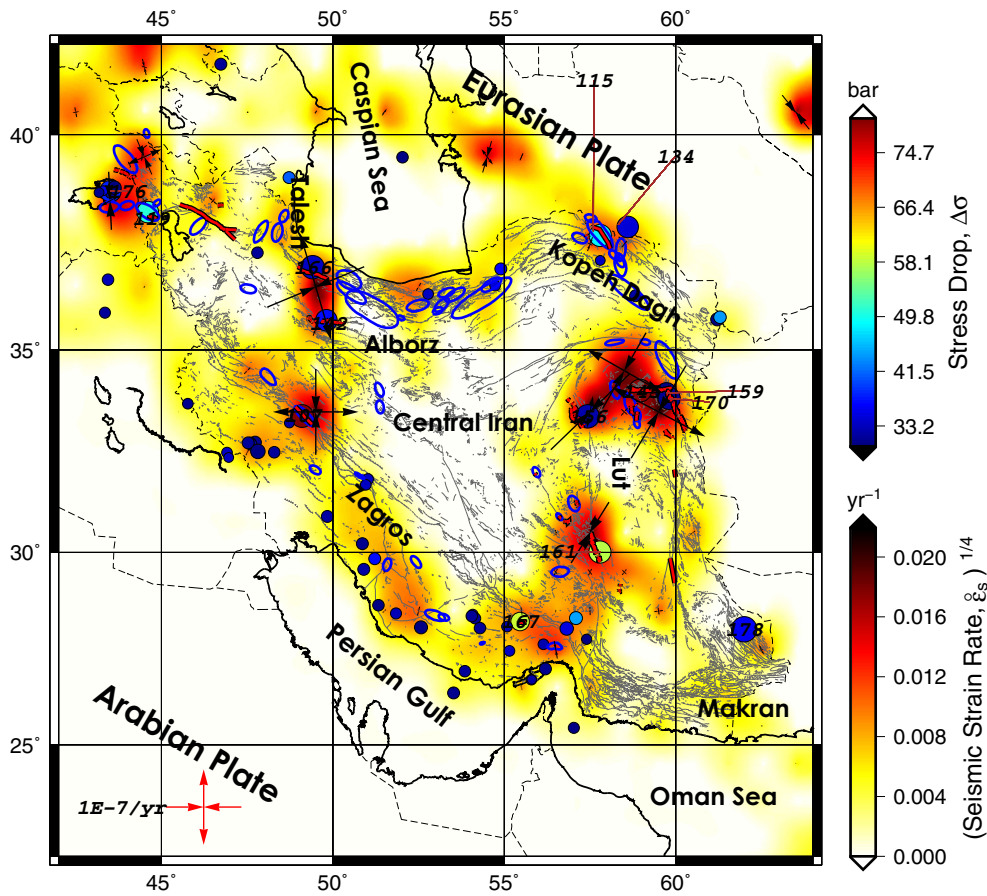


Figure 3

The colored background shows the magnitude of seismic strain rate in the Iranian Plateau due to large earthquakes since 1909. The color is based on the fourth root of seismic strain rate to better show the distribution. The ruptured fault segments (red lines) and macroseismic zones (blue ellipses) are the same as in Fig. 2. The crossing arrows, plotted at grid nodes every 100 km, show the surface projection of principal axes of the seismic strain rate tensor. The missing crosses are due to their small magnitudes. Circles show earthquakes with stress drop larger than 30 bar. The numbering refers to the codes in Table 1

elementary area of the fault surface over which the sources of many earthquakes during a particular time interval are distributed. Earthquakes are related to many irregularly distributed faults and the location precision generally is not accurate enough to be associated with a particular fault. Therefore, it seems reasonable to describe the involved tectonic process as deformation in a volume. Kostrov and Das (1988) used the description presented by Riznichenko (1965), assuming that fractures at the earthquake source are randomly distributed in space, to define the average of the strain rate due to earthquakes as

$$\dot{\varepsilon}_s = \frac{1}{2\mu\Delta V\Delta t} \sum_{k=1}^n M_0^k, \quad (1)$$

where μ is bulk shear modulus, M_0^k is the seismic moment of the k th earthquake of the n earthquakes, ΔV is the volume of interest and Δt is the time interval. Equation 1 gives the magnitude of the seismic strain rate and we can rewrite it for each component of the strain rate tensor as in Masson et al. (2005)

$$\dot{\varepsilon}_{ij} = \frac{1}{2\mu\Delta V\Delta t} \sum_{k=1}^n M_{ij}^k, \quad (2)$$

where M_{ij}^k shows the ij component of the moment tensor for the k th earthquake. We used the focal solutions of larger earthquakes for the period 1909 to 1975 from Jackson et al. (1995) and the Global CMT solutions for the period 1976 to 2016 to calculate the

Table 2

Gutenberg–Richter (G–R) parameters for different seismogenic zones (Fig. 10) in Iran are shown in columns 2–4. SD, N and N_v , respectively, show standard deviation, number of events in each zone, and number of events used in computation of the G–R parameters

Zone	<i>a</i>	<i>b</i>	<i>a / b</i>	SD	<i>N</i>	N_v	Type	Lon.	Lat.	Region	Largest event
1	4.44	0.92	4.84	0.082	234	113	II	49.45	36.72	Rudbar	1983/07/22 (5.6)
2	4.73	0.86	5.47	0.055	642	206	IV	45.44	36.72	Uremieh	1930/05/06 (7.2)
5	3.83	0.77	5.00	0.051	295	141	V	47.83	38.15	Ardabil	0891 (6.3)
6	4.13	0.65	6.39	0.068	1419	689	V	57.33	38.28	Ashkhabat	1895/07/08 (8.2)
7	5.05	0.89	5.65	0.051	662	231	II	48.52	38.37	Astara	1980/05/04 (6.5)
8	3.98	0.73	5.48	0.093	473	329	V	53.11	33.80	Badrood	1977/05/25 (5.4)
9	4.14	0.66	6.31	0.041	320	174	IV	58.25	29.56	Bam	1981/07/28 (7.2)
10	5.10	0.84	6.08	0.158	436	206	II	52.50	27.90	Bushehr	1008/04/11 (6.5)
11	4.57	0.71	6.43	0.092	402	206	IV	53.86	27.36	Bastak	1956/10/31 (6.8)
12	4.21	0.67	6.27	0.060	1311	744	V	56.87	37.33	Bojnurd	1929/05/01 (7.4)
13	3.66	0.59	6.17	0.085	465	304	VI	48.76	33.74	Borojerd	2006/03/31 (6.1)
14	4.07	0.69	5.90	0.036	539	222	II	51.36	30.93	Boroujen	1988/08/11 (6.1)
15	4.13	0.77	5.40	0.082	825	485	III	53.39	36.47	Caspian East	1957/07/02 (7.1)
16	4.51	0.84	5.35	0.043	932	545	II	51.44	36.69	Caspian West	1825 (6.7)
18	3.93	0.78	5.05	0.096	382	278	VI	50.43	34.60	Chahar Taghi	1980/12/19 (6.1)
19	4.04	0.74	5.47	0.043	547	261	II	45.06	38.39	Chalderan	1304/11/07 (6.7)
20	4.29	0.85	5.05	0.051	476	217	II	54.26	36.22	Damghan	1830/04/03 (6.5)
21	3.94	0.85	4.65	0.098	203	148	VI	58.89	34.16	Dasht e Bayaz	1979/11/27 (7.0)
22	4.73	0.75	6.28	0.025	1115	697	IV	48.89	32.60	Dezful	2006/03/31 (6.1)
23	3.79	0.68	5.58	0.065	222	105	I	58.03	34.80	Doruneh	1903/09/25 (6.5)
24	4.48	0.82	5.45	0.063	519	149	II	47.07	33.45	East Ilam	0871/11/18 (6.8)
25	4.40	0.80	5.50	0.187	886	628	V	49.84	35.71	Eshtehard	1962/09/01 (7.2)
26	4.15	0.72	5.80	0.043	541	196	IV	50.13	32.43	Farsan	1977/04/06 (5.9)
27	4.16	0.75	5.57	0.025	1409	661	II	52.38	35.27	Garmsar	0743 (7.2)
28	3.70	0.65	5.69	0.091	273	175	II	58.92	31.85	Ghale Zari	2000/10/23 (5.3)
29	3.91	0.71	5.50	0.050	176	116	V	53.07	28.62	Ghir	1972/04/10 (6.9)
30	3.92	0.79	4.97	0.135	668	370	VII	59.38	32.39	Giv	1987/11/24 (5.3)
31	4.20	0.71	5.93	0.097	497	370	III	53.77	37.42	Gomishan	2004/10/07 (5.6)
32	4.19	0.78	5.38	0.048	679	432	IV	53.28	34.95	Googerd	1993/06/09 (5.0)
33	4.74	0.77	6.15	0.066	969	646	II	55.05	37.18	Gorgan	1890/07/11 (7.2)
34	4.48	0.85	5.28	0.164	568	267	III	54.19	36.15	Qumis	0856/12/22 (7.9)
35	4.55	0.76	5.98	0.034	590	375	II	46.78	32.82	Ilam	1864/12/02 (6.4)
36	4.16	0.77	5.41	0.057	388	171	II	55.98	32.06	Inter Mines	1911/04/18 (6.5)
37	3.53	0.60	5.87	0.040	404	160	II	58.38	35.61	Kadkan	1996/02/25 (5.4)
39	4.26	1.06	4.01	0.089	303	107	I	50.92	35.50	Karaj	1177/05 (7.2)
41	4.14	0.94	4.39	0.069	368	181	II	51.52	33.78	Kashan	1844/05/12 (6.4)
42	3.46	0.61	5.62	0.052	176	110	II	57.46	34.46	Kalmard	1903/09/25 (6.5)
43	4.38	0.72	6.10	0.041	468	234	II	51.25	29.30	Kazerun	2010/09/27 (5.9)
45	3.98	0.67	5.92	0.079	939	593	IV	46.55	34.51	Kermanshah	1975/01/14 (5.1)
46	4.51	0.91	4.94	0.068	372	166	II	56.17	37.89	Khaled e Nabi	1970/07/30 (6.6)
47	4.33	0.75	5.79	0.063	691	402	IV	48.81	32.95	Khoramabad	1976/11/15 (5.4)
49	4.42	0.71	6.24	0.056	882	521	V	56.57	31.24	Kuhbanan	1911/04/18 (6.5)
50	4.16	0.78	5.32	0.062	337	135	VI	55.56	30.37	Bardsir	1923/09/22 (6.9)
51	4.23	0.81	5.22	0.052	300	162	IV	44.54	39.18	Maku	1976/11/24 (7.3)
52	4.26	0.82	5.20	0.050	693	418	II	49.04	34.52	Malayer	2011/09/05 (4.5)
54	4.50	0.70	6.39	0.022	846	552	IV	49.96	30.80	Marun	1988/03/30 (5.7)
56	3.83	0.71	5.36	0.113	519	293	II	53.08	35.85	Mosha East	1990/01/20 (5.8)
57	3.66	0.73	5.00	0.104	437	302	IV	52.06	35.74	Mosha Middle	2006/12/20 (4.2)
59	4.12	0.79	5.24	0.041	1154	351	II	58.71	36.26	Neyshabur	1389/02 (7.6)
66	3.98	0.70	5.70	0.054	622	385	V	49.99	35.21	Qom	2002/06/22 (6.5)
68	4.45	0.84	5.31	0.066	302	154	II	56.89	31.35	Ravar	1911/04/18 (6.7)
70	3.80	0.77	4.96	0.084	321	190	V	52.98	34.76	Rig Jen	1982/10/25 (5.4)
71	3.52	0.63	5.56	0.043	362	179	III	57.50	36.37	Sabzvar	1208/07/16 (6.5)
72	4.68	0.79	5.95	0.030	1417	510	IV	46.41	35.47	Zagros	1963/03/24 (7.2)

Table 2

continued

Zone	<i>a</i>	<i>b</i>	<i>a / b</i>	SD	<i>N</i>	<i>N_v</i>	Type	Lon.	Lat.	Region	Largest event
74	3.94	0.80	4.96	0.038	1143	324	II	59.45	36.85	SE Quchan	1985/08/16 (5.6)
75	4.39	0.84	5.21	0.035	1858	508	III	59.80	36.61	Quchan-Mashad	1895/01/17 (6.8)
76	4.32	0.82	5.27	0.092	280	186	II	57.57	31.67	Shahdad Tabas	1982/12/19 (5.9)
78	3.55	0.79	4.51	0.077	412	278	II	57.97	37.34	Shirvan	1963/03/31 (7.0)
79	4.37	0.67	6.49	0.050	910	573	IV	49.60	31.93	Shushtar	1929/07/15 (6.2)
81	3.99	0.68	5.89	0.040	600	266	V	59.98	30.95	East Lut	1936/06/30 (6.2)
82	4.07	0.77	5.25	0.057	292	133	II	57.29	33.79	Tabas	1978/09/16 (7.3)
83	3.56	0.64	5.61	0.043	494	196	V	46.70	37.98	Tabriz	1721/04/26 (7.7)
87	4.20	1.02	4.12	0.082	590	145	II	58.34	37.15	West Quchan	1895/01/17 (6.8)
90	3.90	0.73	5.37	0.117	449	249	VI	60.04	33.48	Zirkuh	1979/11/27 (7.0)
91	4.61	0.74	6.22	0.037	1357	339	VI	49.66	32.87	Zagros	1909/01/23 (7.7)
93	4.25	0.77	5.49	0.063	224	146	II	54.84	29.03	Zagros	2006/02/28 (6.0)
94	4.44	0.67	6.67	0.119	373	281	IV	51.76	40.57	Caspian	1895/07/08 (8.2)
95	3.83	0.74	5.17	0.047	382	222	II	50.59	36.23	Taleghan	1608/04/20 (7.6)
96	4.34	0.69	6.34	0.026	1065	497	V	49.07	33.17	Zagros	1909/01/23 (7.7)
97	3.84	0.61	6.26	0.034	676	201	IV	50.77	31.95	Zagros	1977/04/06 (5.9)
98	4.66	0.86	5.43	0.054	337	181	II	52.28	38.26	Central Caspian	2012/02/04 (4.8)
99	4.30	0.71	6.04	0.094	240	197	III	49.77	40.04	Baku	1667/11 (6.9)
100	3.83	0.71	5.38	0.059	323	112	II	57.75	33.46	Birjand Line	1978/09/16 (7.3)
102	4.01	0.79	5.07	0.073	376	108	II	60.15	32.43	Tabas Masina	1936/06/30 (6.2)
103	4.78	0.75	6.33	0.048	479	197	II	56.33	27.36	Gheshm	1977/03/21 (6.9)

Types of G–R distribution are shown in column 8 and Fig. 9

Bold values indicate their important

seismic strain rate. We divided the study area into $1^\circ \times 1^\circ$ cells, 20 km thick. We chose this thickness according to the depth distribution of earthquakes in Iran (e.g., Engdahl et al. 2006) and the fact that the dip extent of major earthquakes, primarily strike-slip, derived through waveform inversion requires approximately a 20 km crustal thickness. All the earthquakes located in every cell were used in calculating the seismic strain rate in that cell. Crustal earthquakes whose depths might have reached 30 km also were included in the analysis. We justified this by considering the larger uncertainty of the earthquake depth and the likelihood of rupture extension into shallower depths for those earthquakes.

Figure 3 shows the surface projection of the principal axes and also the magnitude of seismic strain rate associated with the aforementioned earthquakes since 1909.

3.2. Geodetic Shear Strain Rate

We densified the most recently available combined GPS velocity field (1999–2011) reported by

Zarifi et al. (2014) with new published velocities (1997–2008) for eastern Iran (Walpersdorf et al. 2014) to compute geodetic strain rates (Table 3). Similar to Zarifi et al. (2014), the VELROT program (Herring et al. 2010) was used to generate a homogeneous velocity field for this combination in a unique Eurasia-fixed frame based on ITRF2008 (Altamimi et al. 2012). The RMS fit for the 82 components from the 41 common stations, used in both studies, was $0.43 \text{ mm year}^{-1}$. The total number of GPS stations increased from 239 in Zarifi et al. (2014) to 281 stations, which better densified the eastern part of the country (Fig. 4).

We used SSPX program (Cardozo and Allmendinger 2009) to compute infinitesimal horizontal strain rates from GPS horizontal velocities. The SSPX program and its predecessor Strain SimPro have been successfully used in previous studies for deformation analysis of GPS networks (Allmendinger et al. 2007; Unglert et al. 2011; Mullick et al. 2009; Zarifi et al. 2014). Following Allmendinger et al. (2007) and Zarifi et al. (2014), the grid-distance neighbor method was applied to estimate the

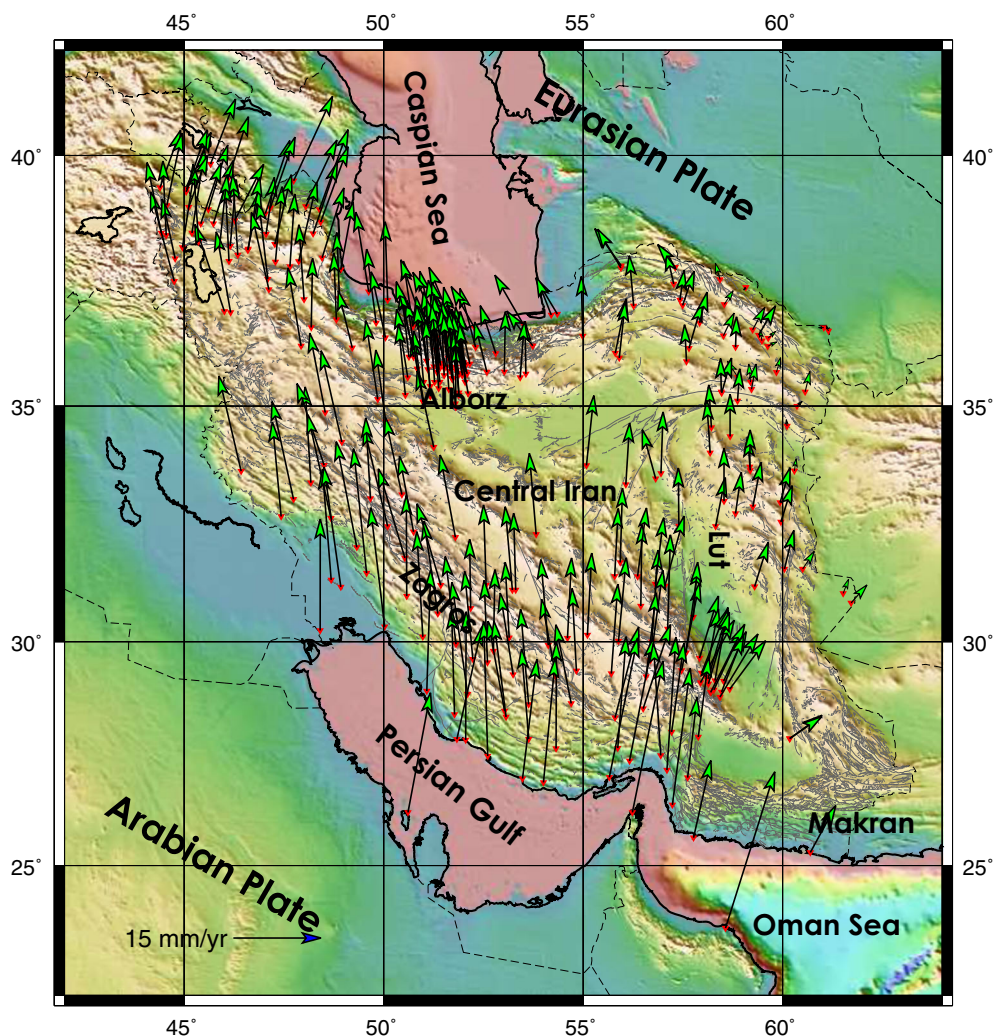


Figure 4

GPS stations and GPS velocity field (in stable-Eurasia fixed frame) in Iran, integrated from Zarifi et al. (2014) and Walpersdorf et al. (2014), (see also Table 3)

heterogeneous tectonic deformation in our study area. The grid-distance neighbor method uses weighted least squared adjustment, where each station is weighted by its distance to the center of the cell: $W = \exp\left(\frac{-d^2}{2\alpha^2}\right)$ where W is the weighting factor, d is the distance and α is a constant that specifies how the closeness of the stations to the center of the cell influences the strain solution. Stations within 1α distance contribute more than 67% to the solution, whereas those at a distance greater than 3α contribute less than 1% (Cardozo and Allemindigner 2009).

Using the SSPX program, we estimated the strain rate at the center of each cell of a $100 \times 100 \text{ km}^2$

rectangular grid by inclusion of 281 Eurasia-fixed GPS velocities, Grid-distance neighbor method and $\alpha = 75 \text{ km}$ (Fig. 5). We also estimated the maximum shear strain rates, the difference of the two principal infinitesimal strain rates (Fig. 6). The orientations of the maximum shear strain rates are always at 45° to the principal axes (Allmendinger et al. 2007). We summarized our geodetic computations in Tables 3 and 4.

The distribution of GPS stations across a number of strike-slip faults in Iran allows for the construction of transects across faults and projecting velocities of the stations inside into fault-parallel and fault-perpendicular components. The velocity profiles

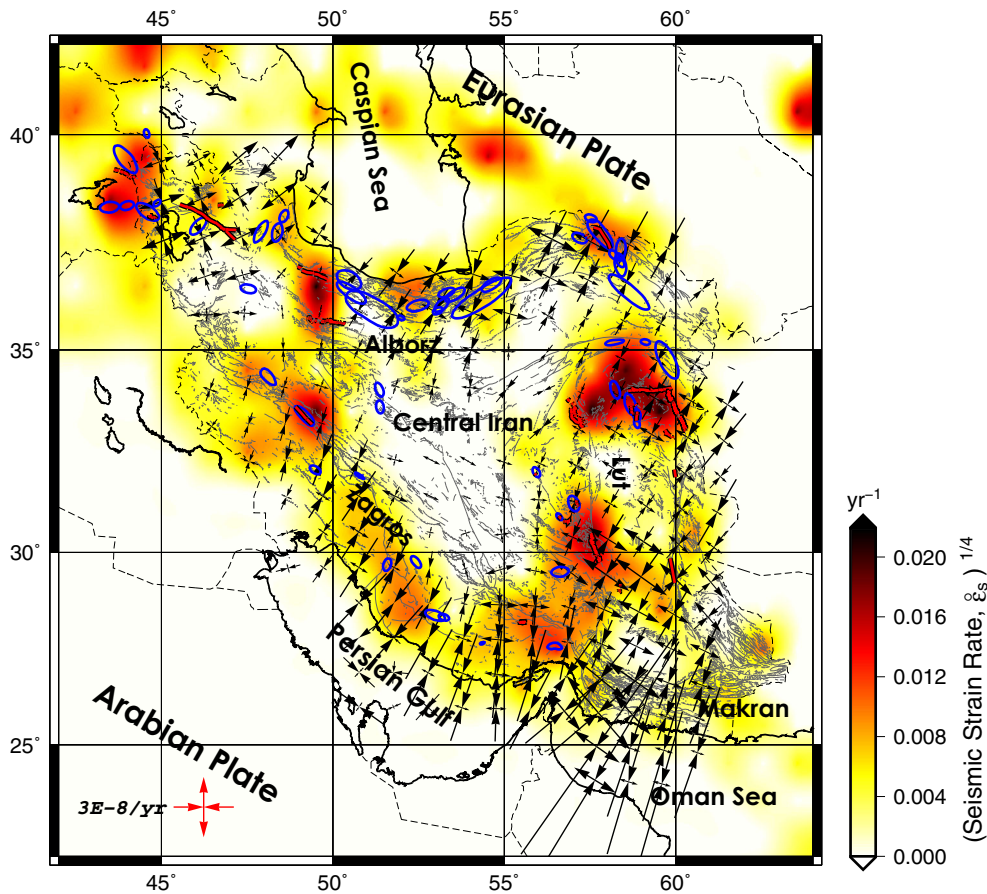


Figure 5

Geodetic strain rates (*crossing arrows*) deduced from our combined velocity field in Iran. The grid cells for calculations of strain rates are rectangles with 100 km dimension (see also Table 4). The *colored background* shows the magnitude of seismic strain rate. The ruptured fault segments (*red lines*) and macroseismic zones (*blue ellipses*) are the same as in Fig. 2

extracted from the stations inside these transects allow us to drive the geodetic slip rates for some strike-slip faults in Iran and compare the rates with geological estimates. However, the accuracy of such geodetic estimations depends on the distribution of GPS velocities in these transects (McGill et al. 2015).

3.3. Static Stress Drop

The static stress drop reflects tectonic unloading (Brown et al. 2015), which can remain almost constant over several orders of magnitude (Lengliné et al. 2014). This is due to the consistent level of differential stress, $\sigma_1 - \sigma_3$, in the vicinity of the rupture area as the main controlling factor in shear faulting. Here, σ_1 and σ_3 represent the maximum and

minimum principal stresses. Therefore, stress drop can be used as an indicator of stress level and its variation shows snapshots of the unloading state at different fault segments. Some generalizations on the variation of stress drop are proposed. Kanamori and Allen (2013) concluded that the stress drop is greater for earthquakes with larger repeat time. Allmann and Shearer (2009) found that strike-slip earthquakes show a three to five times larger stress drop than others. Kanamori and Anderson (1975) demonstrated that stress drop for intraplate earthquakes is larger than those for interplate earthquakes and Allmann and Shearer (2009) claimed a two times larger stress drop for intraplate earthquakes. Zielke and Arrow-smith (2008) numerically showed the temperature dependence of friction and consequently variation of

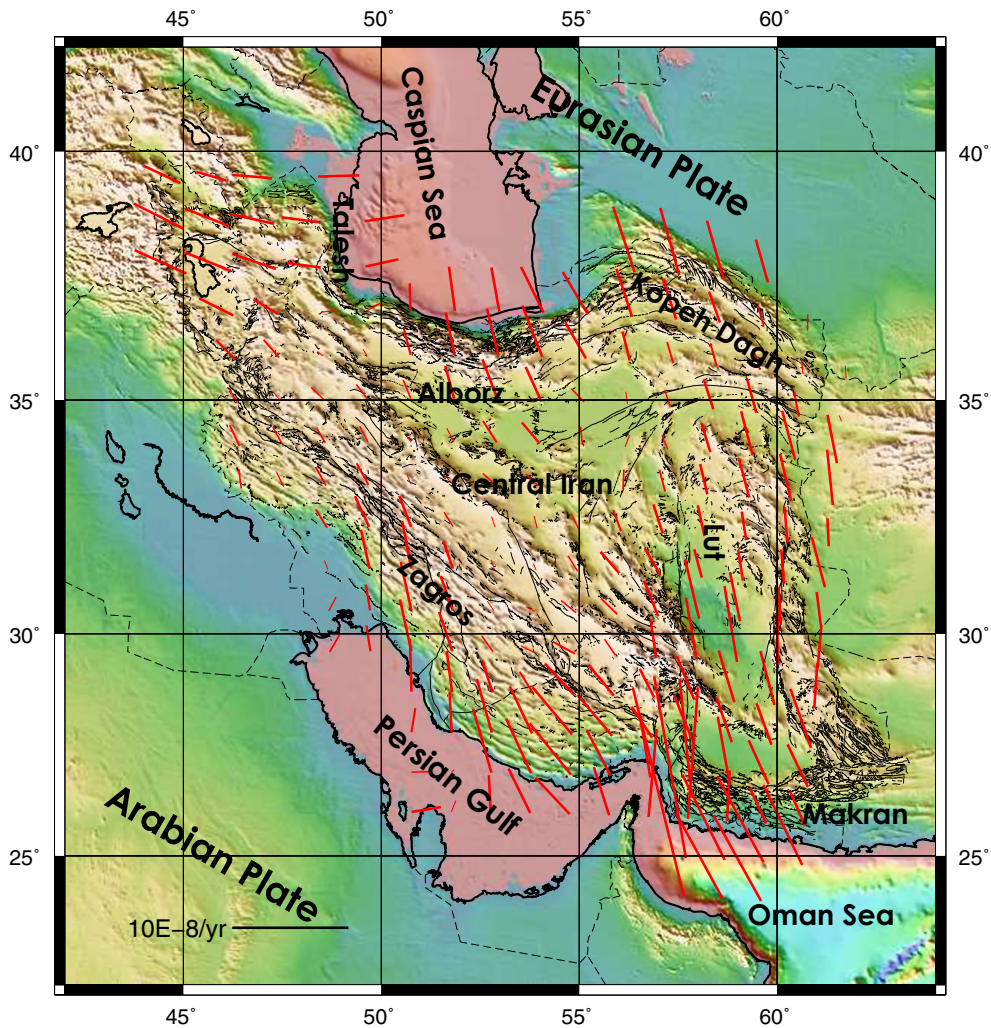


Figure 6

Strike of geodetic maximum shear strain rate in Iran. Geodetic shear strain rates were computed as the difference of the two principal infinitesimal strain rates (see also Table 4)

stress drop with depth. Frohlich (2006) suggested that intermediate and deep earthquakes show an approximately one order of magnitude larger stress drop when compared to shallow events.

Static stress drop $\Delta\sigma$ is proportional to the spatial derivative of slip $\frac{D}{l}$ (Vallée 2013)

$$\Delta\sigma \propto \frac{M_0}{l^3} \propto \mu \frac{D}{l}, \quad (3)$$

where μ is bulk shear modulus, D is average slip and l is a characteristic rupture dimension. The explicit relations for stress drop in terms of seismic moment

M_0 , Lamé parameters λ and μ , rupture length L and rupture width w are expressed as Eqs. 4 and 5, respectively, for strike-slip and dip-slip faulting (Lay and Wallace 1995)

$$\Delta\sigma = \frac{2M_0}{\pi w^2 L}, \quad (4)$$

$$\Delta\sigma = \frac{4(\lambda + \mu)M_0}{\pi(\lambda + 2\mu)w^2 L}. \quad (5)$$

We find Lamé parameters at different depths by interpolating the corresponding parameters from the Preliminary Reference Earth Model (RREM)

(Dziewonski and Anderson 1981). The most accurate stress drop values are found for earthquakes with available surface rupture and slip distribution. These include all the post-1900 earthquakes with $M > 7$ and some other smaller events. For such earthquakes, the variables M_0 , w and L are derived from the slip inversion. For those events without slip distribution or surface rupture, the dimensions L and w can be approximated from the half-duration time t_{hd} . t_{hd} is given in the Global CMT catalog and represents half the duration of the moment rate function (Ekström et al. 2012). Although t_{hd} is assumed for the CMT inversion and is not derived from the analysis, we think that it affects the robust results of CMT inversion and therefore is valid for use here. By assuming average rupture velocity v_r of 2.1 km/s, the length L and width w of the rupture can be computed as

$$\begin{aligned} L &= 2ct_{hd}v_r, \\ w &= \min(2ct_{hd}v_r, \frac{20.0}{\sin(\delta)}), \end{aligned} \quad (6)$$

where δ represents the dip angle and c is a constant that is related to rupture directivity. For a bilateral rupture, assuming all other parameters unchanged, the computed dimension is twice that computed for a unilateral rupture with the same rupture duration. We consider c as 0.75, somewhere between 1.0 for bilateral and 0.5 for unilateral ruptures. We limit the width of the rupture such that it remains in the brittle upper 20 km of the crust.

A number of earthquakes in Iran show stress drop of larger than 30 bar including all the events larger than 7 (Fig. 3). The majority of events show $3 \leq \Delta\sigma \leq 30$ bar (Fig. 8). The computation of stress drop is challenging and different methods may find values that vary by one or two orders of magnitude. This is due to uncertainties in the estimation of rupture dimension. The most accurate values for stress drop can be found if the rupture dimensions are obtained through direct measurements in the field or through well-resolved slip distributions. In such cases, Eqs. 4 and 5 can be implemented directly. We consider stress drop values for 30 earthquakes in Iran, with known rupture dimensions, as a benchmark. Figure 7 shows four differently estimated sets of stress drop. The values found through half-duration method are comparable with the benchmark values. The half-duration

method overestimates the values for larger than seven earthquakes. However, for all such earthquakes the rupture dimensions are available by field measurements and/or slip inversions and we use those dimensions in the computations. Therefore, we consider the computed stress drop values in this article as valid. The P-wave spectra method (Allmann and Shearer 2009) overestimates for all obtained values substantially. The values found through S-wave spectra method (Hassani et al. 2011; Zafarani et al. 2012; Zafarani and Hassani 2013) cover a wide range and it seems that the values for a number of the events are overestimated. In both P- and S-wave spectra methods, the rupture area is found by using Brune's method (Brune 1970).

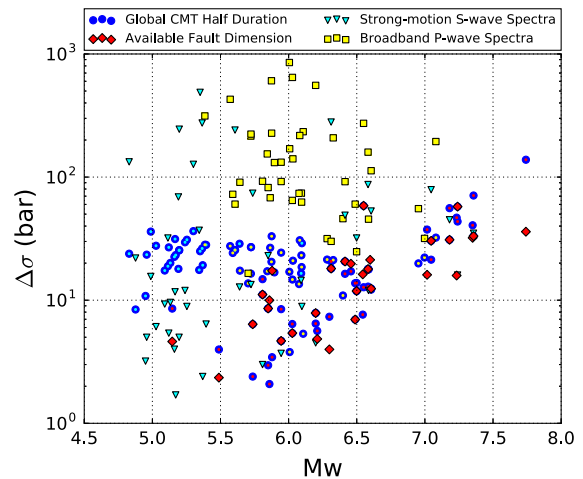


Figure 7

Static stress drop for a number of earthquakes in Iran that are found by using four different methods. The *circles* show the values that are found by using the half-duration data in the Global CMT catalog (Ekström et al. 2012) and by employing the method of Sect. 3.3. The *colored point* inside each *circle* indicates its correspondence to another value that is found by another method which has the *same symbol color* and magnitude. The *diamonds* represent the stress drop for those earthquakes that their rupture dimensions were known through field measurements, slip inversion and aftershock distribution. In such cases, Eqs. 4 and 5 can be used directly. The *inverted triangles* show the values that are obtained by using S-wave source spectra of local strong-motion data (Hassani et al. 2011; Zafarani et al. 2012; Zafarani and Hassani 2013). The *squares* show the values which are found through isolation of P-wave source spectra of broadband data at teleseismic distances (Allmann and Shearer 2009). Any of the earthquakes used in the latter three methods is also used in the first method. However, only some of the earthquakes used in the latter three methods are common

3.4. Gutenberg–Richter Parameters

3.4.1 Basics on Gutenberg–Richter Parameters

Bak and Tang (1989) interpreted the Gutenberg–Richter (G–R) power law distribution as a consequence of the self-organized critical state of the Earth's crust. Such systems evolve toward criticality and display scale invariance near that critical point. Scale invariance shows that the well-constrained regions of the G–R distribution, here the lower-magnitude portion, can be used for estimating the associated parameters. Heimpel (1997) suggested that self-similarity and criticality displayed by a fault during the earthquake cycle can be used to reveal how advanced a fault is within its cycle. Numerically, Heimpel (1997) showed that self-similarity is violated during the early stages of an earthquake cycle and emerges in the later stages. More specifically, the b value of G–R distribution decreases linearly with increasing differential stress, $\sigma_1 - \sigma_3$ (Scholz 2015). The low differential stress at early stages of an earthquake cycle causes failure of small and weak patches. However, larger patches fail at later stages with increased stress. Numerically, this process results in reduction of the b value. Therefore, G–R scaling is more closely approximated during the later stages of the cycle (Heimpel 1997).

The G–R relation may have a predictive dimension provided that the computed a and b parameters represent those for the later stages of the earthquake cycle. Occurrence of a characteristic earthquake on a fault segment marks the end of the cycle for that segment. Assuming $N = 1$, the unique characteristic earthquake in G–R relation, $\log(N) = a - bM$, would have a magnitude of $M_p = a/b$. Here, N is the cumulative number of events, M is magnitude and a and b are the G–R parameters. M_p is the predicted largest earthquake based on G–R relation. This value is small at the beginning of the cycle and increases as the cycle matures.

Perhaps, the a/b parameter is as important as the b parameter for the seismic maturity of a seismogenic zone. Comparison of the a/b value with the maximum expected earthquake based on historical and geological information may reveal the earthquake cycle stage of a fault system. The main

controlling factors on the seismicity are the dimension and strength of asperities. A large, strong asperity behaves differently under stress compared to a number of smaller and weaker asperities. The absence of larger earthquakes results numerically in smaller maximum predicted earthquake, M_p . To clarify this issue, assume a typical G–R distribution with two main deviations. These deviations occur at a lower limit for smaller than threshold magnitudes and at a higher limits for different reasons; e.g., a short catalog span or sparsity of larger events due to the strength and extensiveness of asperities. Practically, we discard the lower limit deviation. However, the higher limit deviations contribute by steepening the G–R fit in the interpolation process. This results in higher b values and also in a smaller magnitude crossing along the magnitude axis.

Smaller values of the maximum predicted earthquake, M_p , are expected at the beginning of an earthquake cycle or during the mature stages of a cycle for strongly coupled and extensive asperities along a fault system. Therefore, a large a/b indicates that the fault system is in its mature stages. However, a small a/b does not necessarily indicate that the fault system is in the early stages of a cycle.

The correlation between low b value areas along a fault system with the location of asperities has been reported for several case studies (e.g. Wyss et al. 2000; Schorlemmer and Wiemer 2005; Wiemer and Schorlemmer 2007; Sorbi et al. 2012; Sukan et al. 2014). Schorlemmer and Wiemer (2005) suggests that b values may act as stress meters for the Earth's crust. Wiemer and Schorlemmer (2007) suggested that low b value ($b < 0.7$) areas in their model for California were more likely to produce large ruptures than high b value ($b > 1$) regions.

The b value increases systematically beyond a critical moment of $M_0 \approx (1.5-2) \times 10^{27}$ dyn-cm, magnitudes of 7.4–7.5, which is attributed to a genuine physical change in the nature and scaling of the earthquake source that is the result of the saturation of the transverse dimension of the fault which cannot be more than the brittle crustal thickness (Okal and Romanowicz 1994). For smaller moments, the associated faulting is considered scale invariant and the observed deviations relative to the G–R curve

(bimodality) may be due in part to the short span of the catalog. Zielke and Arrowsmith (2008) suggested that abrupt increase in rupture width explains the bimodal character of G–R distribution. Abrupt changes in rheology within the seismogenic zone control the depth extent of earthquakes and therefore the deviations in the G–R relation. A characteristic earthquake of the fault system is expected when the rupture width covers the width of the seismogenic zone. Amitrano (2003) experimentally showed that by increasing the confining pressure, the behavior of the rock mass becomes more ductile and the b value decreases. They concluded that the b value is controlled by variations of the internal friction angle induced by changes in the confining pressure. The Mohr–Coulomb failure criterion, $\tau = C + \sigma_n \tan(\phi)$, relates the internal friction angle ϕ , normal stress σ_n , and cohesion C to shear stress τ . Reducing the internal frictional angle decreases the b value and increases the ductile behavior. Another important outcome of reduction of internal friction angle is the development of the bimodal character of the G–R relation [Fig. 9 in Amitrano (2003)].

3.4.2 Gutenberg–Richter Parameters in Iran

High-resolution spatial mapping of the G–R parameters can be achieved using methods such as Wiemer and Wyss (2002), which finds anomalies at the nodes of a grid covering the target area or section. However, we apply the traditional method of estimating the parameters in separate zones which are manually chosen based on the location and extent of known faults or clustering of events along unknown trends. In spatial mapping methods, an earthquake may contribute to the parameter determination of several grid nodes. This may not be the optimal case for a closely spaced fault systems, such as those in this study. A thorough discussion of this and similar issues is given by Kamer and Hiemer (2015). Associating earthquakes with each fault restricts us to use only the recent high-quality data. While the span of time associated with that improved earthquake catalog is much shorter than the return period of the large magnitude events. In this case, we apply it based on the scale invariance of the G–R distributions (Bak and Tang 1989; Heimpel 1997), provided

that the catalog is: 1—complete, 2—contains high-quality small magnitude data only and 3—its duration covers the return period of substantial number of the earthquakes that are used in the parameter estimation.

We used the earthquake catalog of the IRanian Seismological Center (IRSC) for the period 1996–2016 to determine the a and b parameters in the vicinity of different fault systems or earthquake clusters in Iran. The ever-expanding catalog includes more than 96,000 events with magnitude larger than 0.2 as of March 2016. The availability of a fault map in addition to the distribution of the seismic events enables us to determine the proper zonation. However, the catalog includes a substantial number of unreported mine or construction explosions.

We used the “exfilter” tool in the SEISAN computer code (Ottemöller et al. 2013) to remove probable explosions. The tool identifies likely explosions based on normalizing the time of day distribution of seismic events as a function of area. The hourly distribution of the entire catalog indicates that blast activities take place primarily between 06:00 and 16:00 GMT (08:30–18:30 local time). Careful analysis of events in each zone showed that 54 of the 129 zones included explosion activities. The “exfilter” tool marked approximately 16,500 events, 17% of the catalog, as probable explosions. The majority of the removed events fall in the group of events smaller than the completeness magnitudes, about 2–2.5. Therefore, any explosions remaining in the catalog do not effectively contribute to the determination of G–R parameters. The events in the blast-free catalog are almost uniformly distributed over different times of day.

The next preparation step is declustering of the catalog to remove the dependent events, foreshock and aftershock sequences. For this process, we used the Java implementation of the Gardner and Knopoff declustering method (Knopoff and Gardner 1972; Gardner and Knopoff 1974). The declustering process eliminated about 29,700 additional events or about 30% of the entire catalog. In total, 47% of the events were eliminated in the preparation process.

Next, we computed a and b parameters for each zone using a code particularly designed for such a task, “GRTo” (Amorése 2007). GRTo finds the completeness magnitudes automatically. However, in

several cases we assigned larger completeness magnitudes to obtain reliable parameters.

In this study we found seven types of G–R distributions (Fig. 9). The deviations are mainly to the left of the G–R curve and indicate fewer events than the G–R relation predicts. Type I is the most expected but one of the rarer forms, with almost no deviation from the G–R relation. Type II is the most common form and shows minor deviations from the curve. In type III, fewer earthquakes occur at smaller magnitudes than predicted by the G–R relation. However, at larger magnitudes it again follows the G–R relation. Therefore, the deviation is not due to the short span of catalog. Rather, it indicates that some of the cracks preferentially join into larger ones. Types IV and V show significant deviation from the G–R curve which indicates a potential for substantial seismic energy release in the form of type VI. Type VI exclusively represents a fault system that has recently experienced its characteristic earthquake. Although type V shows partial compensation of the deviation with one or more larger events, the fault system has not yet experienced its characteristic earthquake. Except for fault systems with very strong to complete locking, the magnitude of the characteristic earthquake in type VI is approximately one unit larger than that predicted by a/b . Type VII mainly indicates an area where seismicity of more than one fault system contributes to the G–R curve.

Figure 10 shows an a value map for those zones with reliable parameters. We ignored the zones with fewer than 100 events greater than their completeness magnitude. a values greater than 6.5 are found for small zones that are known mining sites. For most of the other zones, the a values range from 2.5 to 5. Figure 11 presents a b value map for the same zones as Fig. 10. While b values larger than 1.2 are found for zones with known mining sites, the majority of the zones show b values in the range 0.5–1.1. Figure 12 shows the a/b map with values generally ranging between 4.0 and 6.7.

4. Discussion

Joint interpretation of variations in the G–R parameters, stress drop, seismic and geodetic strain

rate fields, in conjunction with major historical earthquakes, can provide important information on the stage of maturity for different fault systems in the Iranian Plateau. In particular, negligible seismic strain rate in conjunction with high geodetic strain rate for a region that has not experienced a large earthquake for a long period of time may indicate a seismically mature area. As explained in Sect. 3.4.1, we pay particular attention to areas with larger a/b values.

As expected, we found that high seismic strain rates are associated with the areas which experienced major 7+ earthquakes during the past 100 years. These events show stress drops in the range of 30–80 bar, and most often in the range of 30–40 bar. These values may seem low for intraplate earthquakes, but the strongly shattered brittle crust of the Iranian Plateau, particularly along the existing large fault systems, justifies that level of stress drop. Interestingly, even the major intraplate earthquakes in the subducting Makran slab, e.g., 2013/04/16 (7.7, 178), show stress drop of about 36 bar. This might indicate that earthquakes in the subducting Makran slab also take place along pre-existing weak structures. The largest stress drop, 80 bar, is computed for the 1968/08/31 (7.3, 145) Dasht Bayaz earthquake along the northern bound of the Lut Block. The highest seismic strain rate is in the area of the 1945/11/27 (8.2, 132) Makran interplate earthquake. The coastal area to the west of this earthquake, between 57°E and 64°E, shows very small seismic strain rate that is not comparable to those values in the area of 1945 earthquake (Fig. 3). However, Fig. 5 shows the largest geodetic strain rate of about $1.3E-07 \text{ year}^{-1}$ for the aforementioned coastal area. This slip deficit for the coastal interplate zone eventually will be compensated in the form of a major or great interplate earthquakes. The seismicity in the Makran zone is sparse; however, major extensional earthquakes [e.g., the 2013/04/16 (7.7, 178) earthquake] occur in the subducting slab. The difference between GPS-derived velocities to the west of 61°E along the coasts of the Oman Sea (where overriding and subducting plates meet) indicate partial coupling of the plate interface (Fig. 4). No GPS measurement was available east of 61°E along the Makran coast and the easternmost coast of Oman is at 59.8°E. However, the major

intermediate depth and extensional earthquakes of 2011/01/18 (7.2, 175) and 2013/04/16 (7.7, 178) to the east of 61°E most likely indicate strong coupling in the slab interface.

Further to the north, several major earthquakes, primarily strike slip, ruptured the boundaries of the Lut Block. Earthquakes of 1968/08/31 (7.3, 145), 1978/09/16 (7.3, 156), 1979/11/27 (7.0, 159), and 1997/05/10 (7.3, 170) occurred in the northern part of the Lut block. These earthquakes are located in zones 21, 82 and 90 of b value zones (Figs. 3, 10; Table 2).

Zone 76, with an a/b of 5.3, covers a major strike-slip fault system with conspicuous dislocations along the western boundary of the Lut Block (Fig. 12). The lack of any reported major earthquake associated with this zone is most likely due to the sparsity of the population, the result of its proximity to the Lut desert. The seismic strain rate of this zone is 0.0 year^{-1} (Fig. 3). The geodetic strain rate seems comparatively small, $\sim 1.88\text{E}-08 \text{ year}^{-1}$, at the western bound of the Lut Block (Fig. 5). However, the distribution of GPS stations (Fig. 4) shows that there is no station in this zone and most likely the low values for geodetic strain rate emerge as a result of unconstrained interpolation. The distribution of moderate earthquakes in the last four decades (Fig. 8) shows no earthquakes in this zone. This may indicate strong and extended asperities of the fault system. This is in line with the conspicuous structure of the system. If so, then a moderate a/b value of 5.3 is large enough to conclude that the system is toward the end of its seismic cycle. Type II of the G–R distribution is inconclusive regarding the maturity stage of the zone (Fig. 9; Table 2).

The eastern side of the Lut Block is bounded by a major strike-slip system covered by zones 81 and 102 with a/b of 5.9 and 5.1 respectively (Fig. 12). The respective b values of the zones are 0.68 and 0.79 (Fig. 11). Although the seismic strain rate for these two zones are very small ($\sim 1.0\text{E}-10 \text{ year}^{-1}$, Fig. 3), the geodetic strain rate ($2.0\text{E}-08 \text{ year}^{-1}$, Fig. 5) shows substantial aseismic deformation.

The stress drop values for moderate earthquakes along these zones are in the range of 25–30 bar (Fig. 8), which suggests the potential for larger earthquakes with large stress drop. These values are comparable with the stress drop of the 1997/05/10

(7.3, 170) earthquake, 31 bar, which occurred along the northern part of the same fault system. Ambraseys and Melville (1982) reported approximately 2 years of aftershocks for the 1838 (7.?, 73) earthquake. The northern limit of the surface rupture of the 1838 earthquake extended to approximately 30°N. The distance between the northern limit of the surface rupture of the 1838 earthquake and the southern limit of the surface rupture of the 1997/05/10 (7.3, 170) earthquake is approximately 360 km. Based on the rupture lengths of the other major earthquakes around the Lut Block, this seismic gap may rupture in four to five major earthquakes along the eastern boundary of the Lut Block. The high a/b value of Zone 81 and its G–R curve of type V (Fig. 9; Table 2) suggests that the zone is in the mature stage of cycle. Although major strike slip faults cut through alluvium in Zone 102, there is no report of recent or historical earthquakes in this zone. Despite its moderate a/b value of 5.1, it may be in the final stages of its earthquake cycle. The successive rupture of the 1968/08/31 (7.3, 145), 1979/11/27 (7.0, 159) in Zone 21 and the 1979/11/14 (6.6, 158) and 1997/05/10 (7.3, 170) earthquakes in Zone 90 suggests that rupture of the major strike-slip fault system in Zone 102 is very likely.

Zone 28, with b and a/b values of 0.65 and 5.69, respectively, is mature enough to generate earthquakes of about 6.5 to 7 (Figs. 11, 12).

The southwestern boundary of the Lut Block ruptured in 1981/06/11 (6.7, 160) and 1981/07/28 (7.2, 161) earthquakes located in the northwestern part of Zone 9 with high a/b value of 6.3 and b of 0.66. About 2000 of the 3000 fatalities of the 1981/06/11 earthquake were in the town of Sirch, with a total population of 3500 (Adeli 1982). The southern part of this zone ruptured during the 2003/12/26 (6.6) Bam earthquake, with 26,271 fatalities. The unbroken segment between these two earthquakes may rupture in a single earthquake in a sparsely populated region. It is unlikely that the moderate 2003 Bam earthquake released the entire stored energy of the main fault system. This hypothesis is supported by the fact that the causative fault of the 2003 Bam earthquake, with minor surface expression, was located approximately 5 km to the west of the main fault system in the region. That main fault system did not rupture during

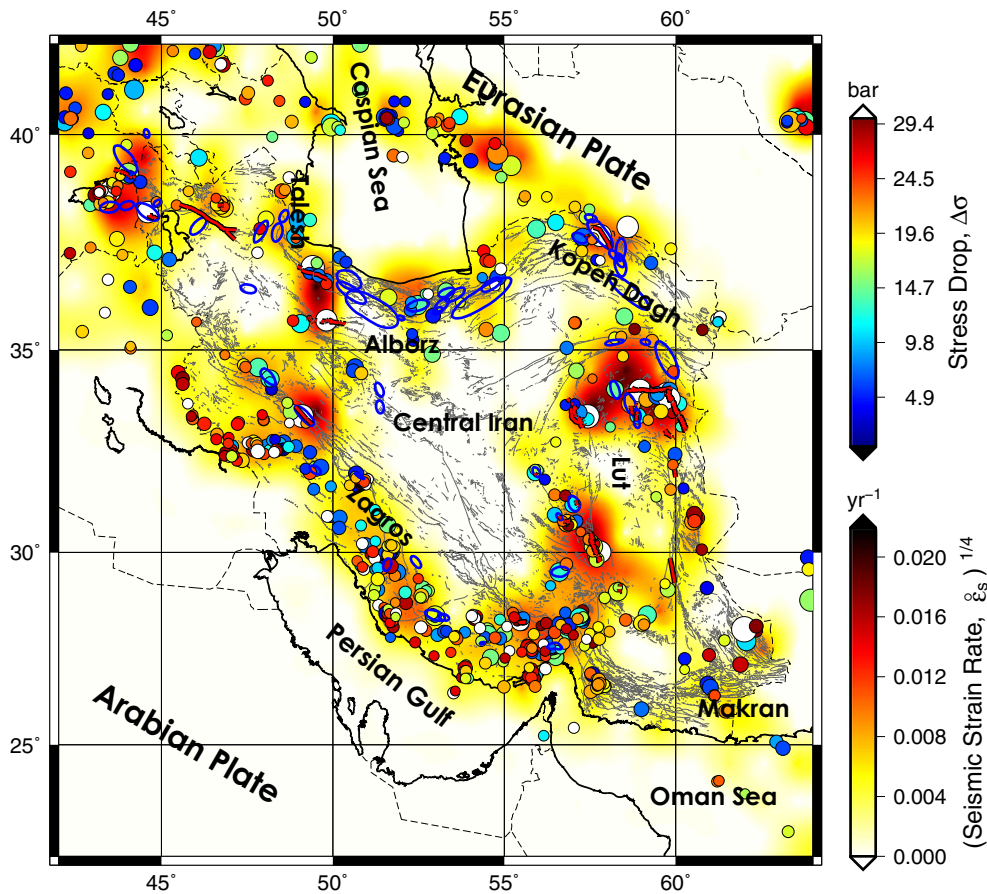


Figure 8

The circles show earthquakes and are colored based on their stress drop level. The white circles represent earthquakes with $\Delta\sigma \geq 30$ bar and are shown separately in Figure 3. The colored background shows the fourth root of the magnitude of seismic strain rate. The ruptured fault segments (red lines) and macroseismic zones (blue ellipses) are the same as in Figure 2

the 2003 earthquake. However, very large surface deformations from past historic events are readily observable in the local alluvium on low-resolution satellite images (Talebian et al. 2004; Nakamura et al. 2005) provide strong evidence for its seismic potential. The relatively low stress drop of the Bam earthquake (18 bar) and the low seismic strain rate ($\sim 1.8E-08$ to $4.8E-11$ $year^{-1}$, Fig. 3), in contrast to the substantial geodetic strain rate for Zone 9 ($\sim 3.5E-08$ $year^{-1}$, Fig. 5), also support this conclusion.

Zone 49 covers the 300 km-long Kuhbanan fault system which hosted the 1933/11/28 (6.2, 123) Bahabad, 1977/12/19 (5.8, 155) and 2005/02/22 (6.4, 174) Zarand earthquakes. The type V G–R curve for this region, together with the high a/b value of 6.2

and b value of 0.71, suggest that this zone is in the mature stage of the earthquake cycle and may experience earthquakes of $M > 6.2$ (Table 2; Fig. 9). An unusual feature of the pure right-lateral 1977 earthquake is its coseismic surface rupture, approximately 19.5 km long, with minor dislocation of less than 20 cm (Berberian et al. 1979). Assuming an average slip of about 15 cm suggests a maximum width of about 10 km. This indicates that the upper half of the brittle crust has ruptured. However, this needs to be verified by slip modeling. If true, then the rupture of the 1977 earthquake should be considered part of the process of the next major earthquake. Due to the remoteness of the region, there is a lack of documentation on historical earthquakes. However, there is a legend about a destructive earthquake that ruined Kuhbanan

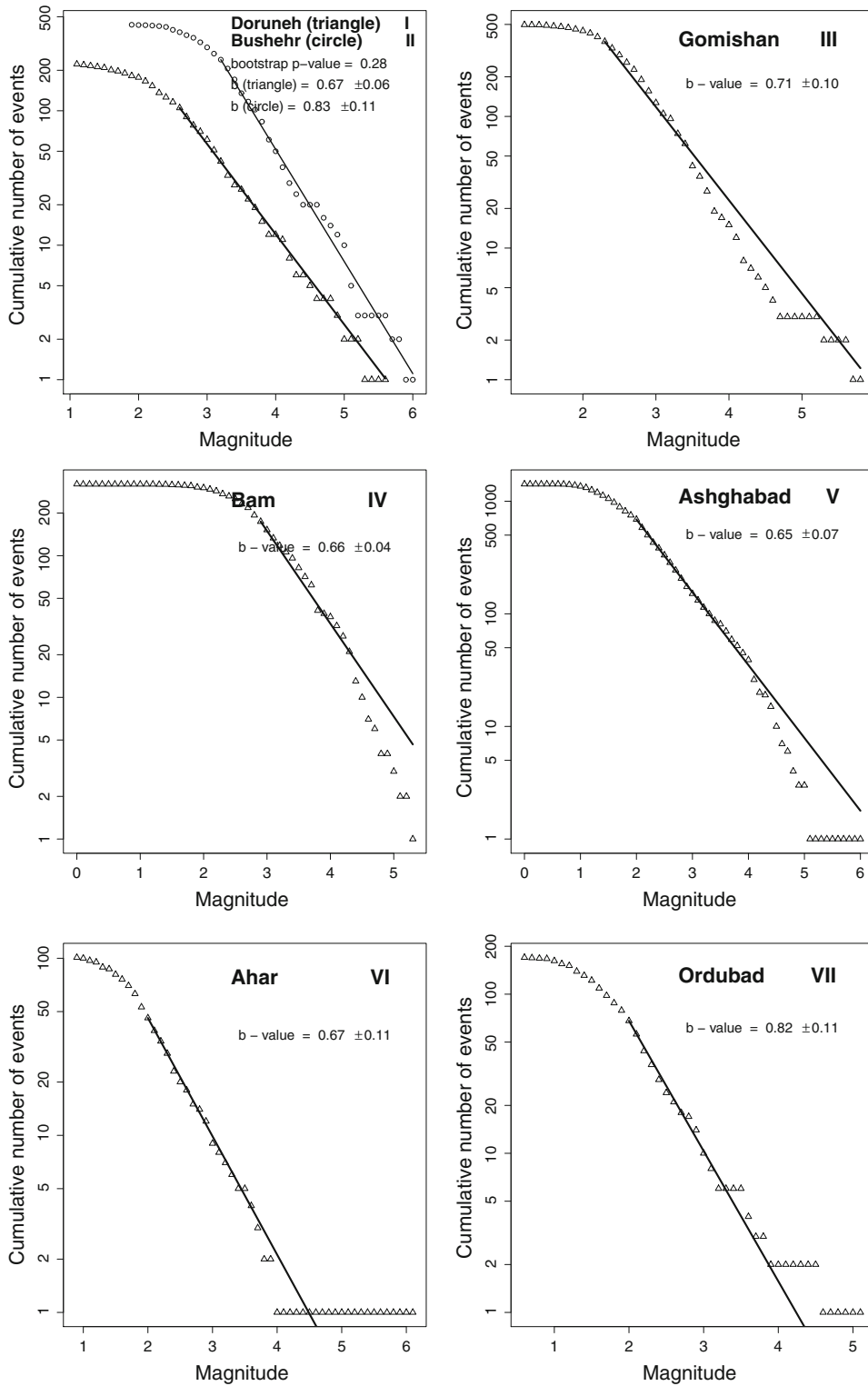


Figure 9

Different types of G-R distribution found by analyzing earthquakes recorded by the IRSC during the period 1996 to 2016. The Roman numbering to the top right of each panel shows the type

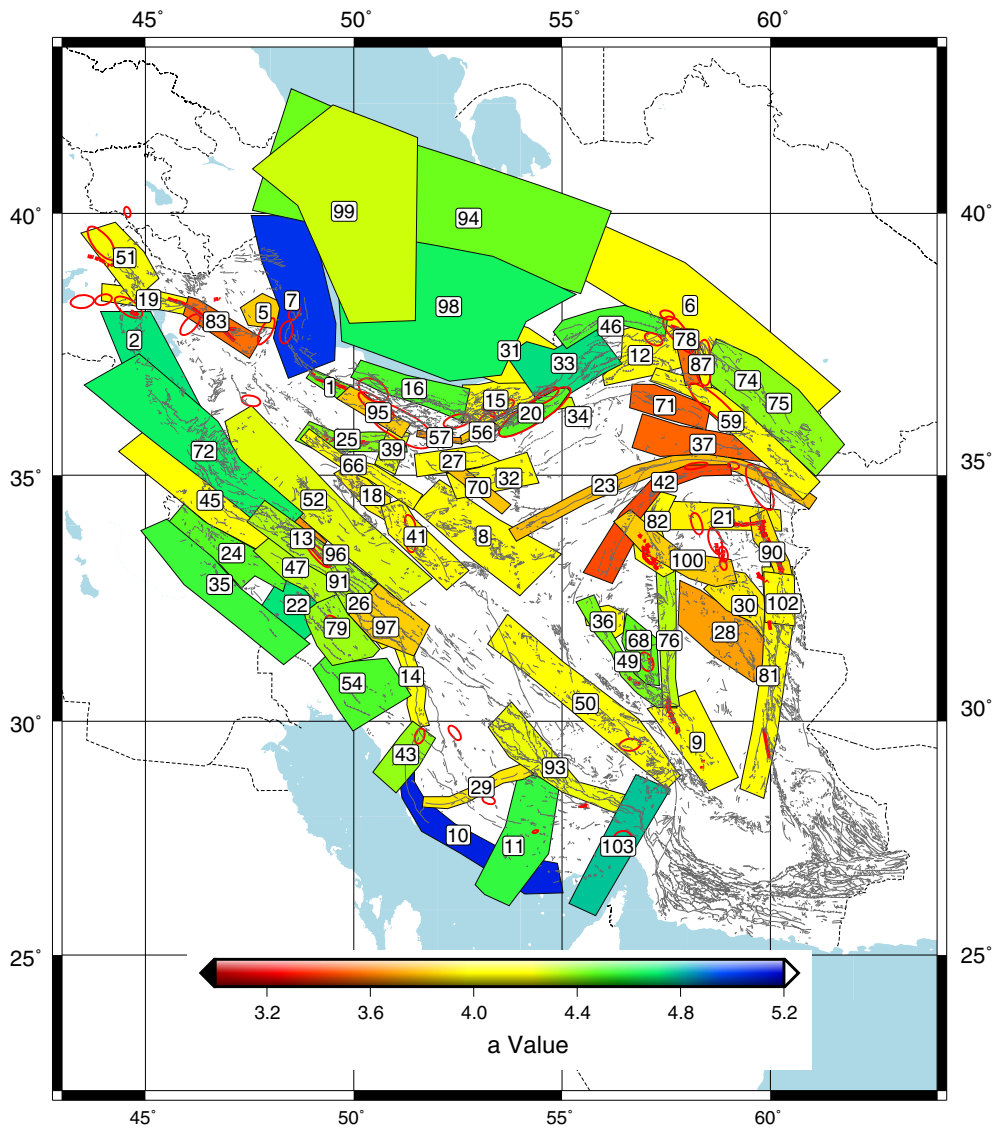


Figure 10

a values of Gutenberg–Richter relation at different zones in Iran computed from the IRSC catalog. The zones with more than 100 earthquakes larger than their corresponding completeness magnitude are shown. The numbers in each zone correspond to the numbering in Table 2. The thin gray line segments show the known faults

sometime in the twelfth century (Ambraseys and Melville 1982). Several moderate right-lateral earthquakes have ruptured the southern half of the Kuhbanan fault system over the last 26 years. The pattern of moderate earthquakes in this region align along the Kuhbanan fault system; however, they show less than 20 bar of stress drop (Fig. 8). The seismic strain rate along the zone is minor ($\sim 5.0\text{E}-09 \text{ year}^{-1}$, Fig. 3), while the geodetic strain

rate is moderate ($\sim 2.0\text{E}-08 \text{ year}^{-1}$, Fig. 5). The distribution of GPS stations suggests that the estimated geodetic strain rate is properly constrained (Fig. 4).

The SE–NW trending zones of 50 and 52 (Fig. 10) and those in Central Iran (zones 8, 18, 27, 32, 39, 41, 66 and 70) show small a/b values (Fig. 12). Zones 50 and 52 correspond to part of the forearc of an ancient subduction zone. The other aforementioned

zones are located within the backarc of the same subduction zone. All these zones have a low level of seismicity, negligible seismic strain rate for those events used in our calculation ($\sim 0.0E+00 \text{ year}^{-1}$, Fig. 3) and a small geodetic strain rate ($\sim 1.0E-08 \text{ year}^{-1}$, Fig. 5).

As a collision zone that emerged from closure of the Neotethys, the Zagros Mountains have a high level of seismic activity. However, due to the presence of incompetent and mobile layers in most parts of the sedimentary cover of Zagros, the deformation is mainly in the form of ductile folding and the brittle part is characterized by frequent small and considerable moderate earthquakes (Berberian 1995; Bahroudi and Koyi 2003; Nissen et al. 2014). The seismic strain rate for Zagros is very low (Fig. 3), while a substantial geodetic strain rate is measured, particularly to the east of 49° . Major earthquakes are missing in the folded region away from the collision front, the Folded Zagros (e.g., zones 4, 10, 11, 22, 24, 29, 35, 43, 45, 59, 74 and 79). However, the High Zagros (e.g., zones 96 and 97) next to the collision front has experienced 7+ earthquakes.

Zone 96, with a b value of 0.69 and an a/b value of 6.34, covers the macroseismic area of the 1909/01/23 (7.4, 107) Silakhur earthquake, with 6000 to 8000 fatalities (Figs. 11, 12). The 1957/12/13 (6.5–7.0, 138), 1958/08/16 (6.7, 139) and 2006/03/31 (6.1) earthquakes occurred to the northwest of the 1909 earthquake. Approximately 180 km to the southeast of the 1909 earthquake, the 1977/04/06 (6.0, 154) Naghan earthquake, with a dominant strike-slip mechanism, occurred in Zone 97 with a b of 0.61 and an a/b of 6.26. In addition to their G–R distributions of type V and IV, the high a/b values for zones 96 and 97 indicate the seismically mature stage of these zones. The strike-slip earthquakes in this region are associated with the right-lateral system of the Main Recent Fault (MRF) with a NW–SE trend. The 1977 Naghan earthquake indicates that the MRF extends to at least 51°E , where it joins the almost N–S right-lateral fault system of Kazerun. The Kazerun fault is located primarily in zones 14 and 43, with respective a/b values of 5.9 and 6.1. The respective b values of the zones are 0.69 and 0.72 (Fig. 11). We found the fault-parallel geodetic surface velocity of $3.13 \pm 1.16 \text{ mm year}^{-1}$ for the Kazerun fault and 3.48 ± 0.69

mm year^{-1} for the MRF system. It is likely that the Kazerun fault system delimits the SE end of the MRF. The similar characteristics of the Kazerun and MRF fault systems suggest that they can be considered as part of one system. Tavakoli et al. (2008) and Authemayou et al. (2009) suggested that the strike-slip motion is distributed from the MRF to the Kazerun system.

The 1909 Silakhur earthquake was along the strike-slip system of MRF. However, the associated surface rupture had an average of 1–2 m of vertical displacement with the northeastern side down-thrown and no indication of strike-slip displacement (Ambraseys and Melville 1982). Since normal faulting is unlikely, we interpret the relative vertical displacement as reverse faulting, which is consistent with the compressional system. The seismic strain rate for the region of the 1909/01/23 (7.4, 107) earthquake, as shown in Fig. 3, is representative of a strike-slip system. This can be reliable if the mechanism of the 1909 event, the main contributor to the seismic strain rate, is strike-slip as interpreted by Jackson et al. (1995).

The known strike-slip events along the MRF are typically less than magnitude 7 and the larger events may not be purely strike-slip. Zones 96 and 97 are the location of the highest peaks in the Zagros Mountains (Fig. 13). This is consistent with the uplift of the southwestern side during the 1909 earthquake. The strike-slip system cannot explain these high peaks. Therefore, we suggest that earthquakes as greater than or equal to the magnitude of the Silakhur event should be expected, particularly to the southeast of that earthquake. The process behind the uplift of this section of Zagros causes extensive tight folding in the neighboring zones of 54 and 79 that also have high a/b values of 6.4 and 6.5, respectively. The respective b values of the zones are 0.70 and 0.67 (Fig. 11). However, the events in these two zones show the lowest stress drop in the Iranian Plateau, approximately 5 bar, while Zone 79 hosts the most active earthquake swarm activity in Iran (Fig. 8). The low level of stress drop for these two zones may show that earthquakes within the zones fall short of magnitudes larger than 7. Zones 22 and 35, located to the west of Zone 79, have significantly different values for stress drop. Earthquakes in Zone 22 have a stress

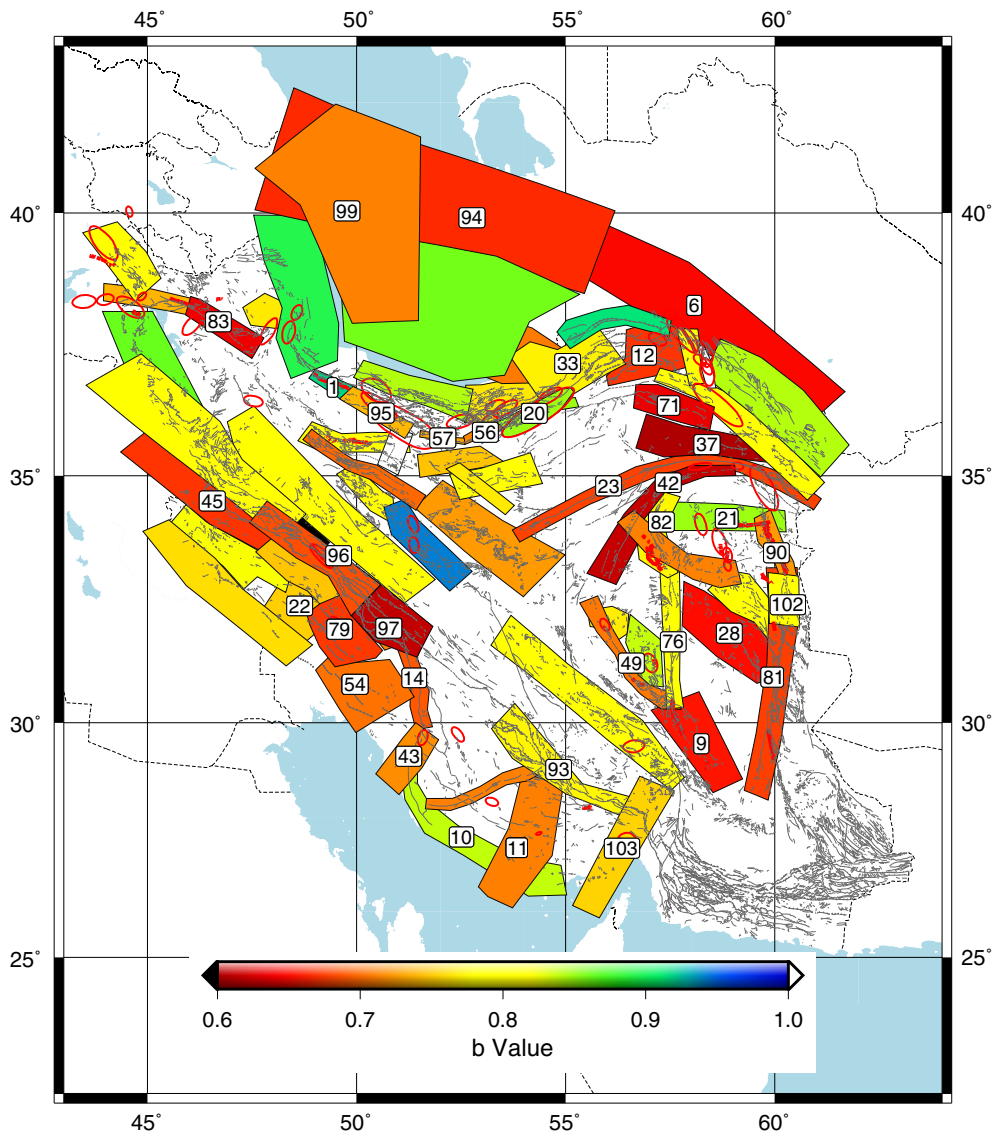


Figure 11
b values of the G–R relation at corresponding zones shown in Fig. 10

drop of 5–15 bar, while all earthquakes in Zone 35 have a stress drop in the range of 25–30 bar. Their a/b values are 6.28 and 5.98, respectively.

Zone 45, which covers the northwestern portion of the MRF, has b and a/b values of 0.67 and 5.92, respectively. This indicates maturity of the zone for generating earthquakes of magnitude 6.5–7 (Fig. 11, 12).

Zone 11, with a b value of 0.71 and an a/b value of 6.4 (Fig. 11), hosts a large number of salt domes. However, the largest salt domes of Zagros are located

to the east, parallel to and outside of Zone 11. No historically damaging earthquake of 7+ has been reported in this zone, but the 1960/04/24 (5.9, 140) Lar earthquake took more than 1300 lives. The 1961/06/11 (6.4) event occurred less than 10 km to the north of the 1960 event.

The largest known earthquake in Zone 103, with an a/b value of 6.3, is the 1977/03/21 (6.9, 153) Khurgo event with 167 fatalities. The zone is located in the southeastern part of Zagros and has experienced a number of 6+ earthquakes and is likely to

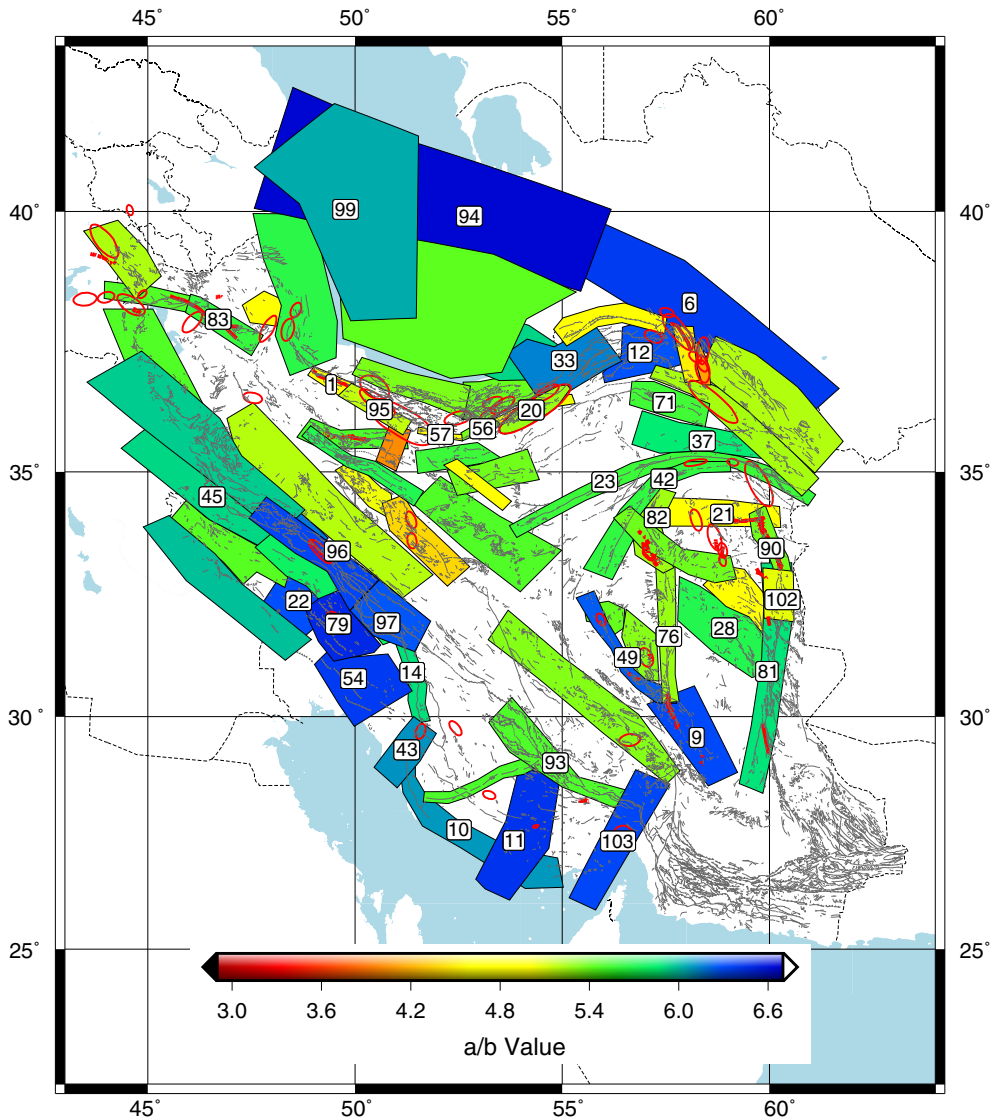


Figure 12
 a/b values at different zones corresponding to those in Figs. 10 and 11

experience more earthquakes of magnitude 6 to 7. The geodetic strain rate along this zone is as large as $\sim 4.5E-08 \text{ year}^{-1}$.

Zones 6 and 94, with a/b values of 6.4 and 6.7, respectively, delimit the Eurasian plate to the north from the Iranian plate (Fig. 12). The respective b values of these zones are 0.65 and 0.67 (Fig. 11). Zone 6 covers the macroseismic area of the 1948/10/05 (7.3, 134) Ashkhabad earthquakes that resulted in at least 110,000 fatalities. The 1946/11/04 (7.5, 131) earthquake occurred in the eastern part of Zone 94,

while the 1895/07/08 (7.4, 94) Uzun-Ada (Turkmenistan) earthquake also caused a tsunami in the Caspian Sea (Kondorskaya and Shebalin 2010; Ambraseys 1997). The most recent major event in the eastern part of Zone 94 is the 2000/12/06 (7.0, 171) earthquake. Therefore, it is reasonable to expect events of this size for the unruptured segments along the system.

Koppeh Dagh, with many historical earthquakes, is located to the south and next to the boundary between the Eurasian and the Iranian plates (Ambraseys and

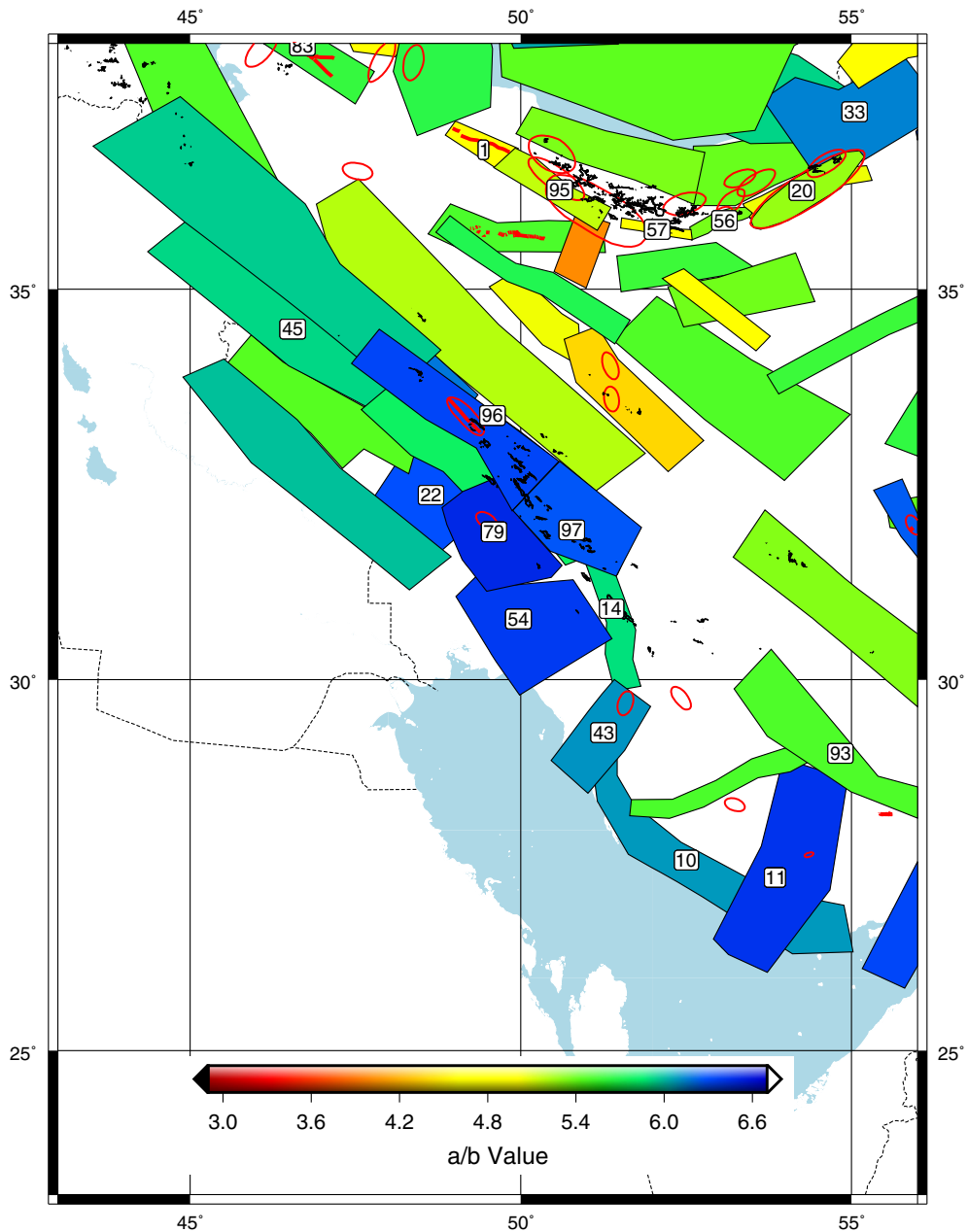


Figure 13

Elevation contours of 3200 m, irregular small *black patches*, shown on the a/b map. The contours in zones 14, 96 and 97 represent the highest peaks in the High Zagros. The other set of these contours locate in the West Alborz along zones 57 and 95

Melville 1982). Zones 12 and 33 have significant a/b values of 6.3 and 6.0, high geodetic strain rate, $\sim 3.0E-08 \text{ year}^{-1}$, and negligible seismic strain rate based on our calculation. The respective b values of the zones are 0.67 and 0.77 (Fig. 11). Geological maps show that north dipping thrust faulting is the

main mechanism in these two zones (e.g., Berberian 1976). While these results indicate the maturity of the earthquake cycle in this zone, no major earthquakes have been reported for these two zones. Zone 59, with an a/b value of 5.2 (Table 2), is the location of four major earthquakes in 1209 (7.6, 35), 1270/10/07

(7.1, 36), 1389/02 (7.6, 41) and 1405/11/23 (7.6, 42). The relatively short time interval between these four major earthquakes is similar to the successive rupture of different segments of a strike-slip system. However, both strike-slip and thrust faults exist in the vicinity of Neyshabur valley. It seems that at least the major portion of the causative fault system ruptured during these four earthquakes over a time window of about 200 years. Shabanian et al. (2012), using geological and morphological evidence, found slip rates of 2.4 ± 0.5 and 2.8 ± 0.6 $mm\ year^{-1}$ for right-lateral and reverse components of active faulting in Neyshabur region. Our GPS-derived right-lateral slip rate along the Neyshabur fault is 2.5 ± 0.9 $mm\ year^{-1}$, which is consistent with the geologically derived value. We expect an average slip of approximately 2–3 m for these major earthquakes. Assuming that part of the GPS-derived motion contributes to aseismic deformation (Table 3 in Khodaverdian et al. 2015), the slip deficit in this zone does not seem to be large enough for recurrence of the aforementioned four earthquakes.

The four neighboring zones of 71, 37, 23, and 42 have very low b values of 0.63, 0.6, 0.68, and 0.61 respectively, which are among the lowest values in the Iranian Plateau (Figs. 11, 12). However, moderate a/b values in the range of 5.56–5.87 are found for these zones. Zone 23 encompasses part of a major left-lateral fault system, Doruneh–Herat, which runs from Central Iran to Central Afghanistan. The seismicity along the system is low and the geodetic strain rate is smaller than that of Kopeh-Dagh in north and Lut to the south. Most likely, the poor GPS station distribution around the fault resulted in unconstrained interpolation (Figs. 4, 5). The damaging historical and recent earthquakes along the fault include 1618/12/19 (? , 50), 1903/05/25 (6.5, 105) and 1923/05/25 (5.7, 109) events. Because there is virtually no settlement in the western part of the system as it passes through the desert, the resulting sparse population may explain the absence of documented historical earthquakes for Zone 23. Based on the morphology of the fault system, major earthquakes are expected here. Zone 42 covers the right-lateral basement fault system of Kalmard. The seismicity in Zone 42 is low and no historical earthquakes are reported for this sparsely populated zone. Based on

the low b values and moderate a/b values for these zones, we suggest that they are mature for generating earthquakes of about 6.5–7.

The overlapping zones of 20 and 34, with a/b values of 5.05 and 5.28, cover the macroseismic area of the devastating 0856/12/22 (7.9, 17) Qumis earthquake (Ambraseys and Melville 1982). The low to intermediate a/b values here are inconclusive with regard to the maturity of the zones, unless the fault systems are strongly coupled. Types II and III of the G–R distribution (Fig. 9) do not hint at the maturity of the zones. However, the slip deficit suggests differently. The magnitude of the 0856 Qumis earthquake, the extent of its devastation and the bending of the causative fault segments in the middle of the macroseismic area, all suggest that strike-slip fault segments with different geometries were involved. This can occur when fault segments with different return periods synchronize and suggests that the next major earthquake in these zones may occur sooner than expected, as a result of separate rupture of the segments, from the return period of a 7.9 earthquake but with smaller magnitudes. The left-lateral GPS-derived velocity for the macroseismic area of the 0856 Qumis earthquake, Zone 20, is 4.5 ± 0.8 $mm\ year^{-1}$, based on our analysis. We also found a similar value of 4.5 ± 1.1 $mm\ year^{-1}$ for the larger strip from 52.6°E to 57.0°E covering zones 20 and 34. Mousavi et al. (2013), using a GPS network in NE Iran, found a left-lateral slip rate of 4–6 $mm\ year^{-1}$ for the eastern Alborz, which includes the macroseismic area of the 0856 Qumis earthquake. In a paleoseismology study of a single trench along the bending fault system, Hollingsworth et al. (2010) proposed that a rupture occurred prior to 1300 A.D. and significantly later than 600 B.C., which is consistent with the 0856 earthquake. The GPS-derived velocity results in more than 5.2 m of slip deficit since the 0856 earthquake. However, part of the deficit is accommodated by aseismic deformation. Khodaverdian et al. (2015) found that seismic deformation constitutes 78–92% of deformation in Alborz, 62–94% in Kopeh Dagh and 28–39% in Zagros. Intuitively, the deformation along the strike-slip systems that are not involved with folding should include less aseismic deformation. We expect variable coupling along this fault system that, assuming

an average coupling of 75%, results in about 4 m of net slip deficit. This is a large value and points to the maturity of the fault system, particularly if, as discussed above, the segments rupture separately.

Zones 1 and 95 in the West Alborz, with a/b values of 4.84 and 5.17, respectively, are the location of major, devastating earthquakes. The b values are 0.92 and 0.74, respectively (Fig. 11). Zone 1 experienced the 1990/06/20 (7.4, 166) Rudbar earthquake, with about 50,000 fatalities (Berberian et al. 1992; Gao and Wallace 1995; National Geophysical Data Center, NOAA 2016). The last known devastating earthquakes in Zone 95 are the 0958/02/23 (7.7, 23) and 1608/04/20 (7.6, 49) Taleghan earthquakes (Ambraseys and Melville 1982). The elongation of macroseismic areas of these two earthquakes and their correspondence with strike-slip fault segments suggest that these events were strike-slip, similar to the 1990 Rudbar earthquake (Fig. 2). The relatively low a/b value for Zone 95 is inconclusive with regard to the maturity of the zone. The area surrounding the surface rupture of the 1990 Rudbar earthquake, Zone 1, is poorly covered by GPS stations and the few GPS measurements show fault-parallel surface velocity of $1.62 \pm 0.6 \text{ mm year}^{-1}$. The macroseismic area of the 0958 earthquake, Zone 95, is covered by more GPS stations. However, the fault-parallel strike-slip component of surface velocity is inconclusive. Djamour et al. (2010) found 1 and 2 mm year^{-1} of strike-slip surface velocity for the southern edge and the northern edge of the mountain range in West Alborz.

The negligible fault-parallel surface velocity may indicate full locking along the main strike-slip system that passes through zones 1 and 95. However, a dense near-fault network of GPS stations is necessary to determine the locking condition (Meade and Hager 2005; Walters et al. 2014; Yamasaki et al. 2014). Nevertheless, the small fault-parallel velocities show that the system is in the latter stages of the earthquake cycle. Savage and Prescott (1978) illustrated, based on the analytical work of Nur and Mavko (1974), that rapid postseismic deformation occurs in the early stages of an earthquake cycle, while strain accumulation is concentrated in later stages. A rare observation of the numerical results of Savage and Prescott (1978) is the GPS data before and after the

1999/08/17 (7.5) Izmit and 1999/11/12 (7.2) Düzce earthquakes in Turkey, which revealed a preseismic strain localization within about 25 km of the fault and a rapid postseismic transient (Yamasaki et al. 2014).

The very low seismicity along the macroseismic areas of the 0958 and 1608 earthquakes supports the strong locking conclusion. Another indicator of full locking of the system is the aftershock distribution of the 1990/06/20 Rudbar earthquake. Aftershocks of this event were mainly located to the north of the surface rupture and abnormally distributed for about 90 km to the north and perpendicular to the surface rupture. Intuitively, the interseismic strain is distributed primarily in the block under stress. Slip deficit, with its maximum on the fault plane, extends to larger distances away from the fault plane in the case of stronger locking. This mechanism causes the interseismic and postseismic processes, including aftershock activity, to extend far from the shear zone, which is the fault plane. This mechanism may explain other observations such as severe water level change in the Caspian Sea before or after each of the three aforementioned earthquakes (Ambraseys and Melville 1982). However, this should be scrutinized carefully in the future.

The strike-slip earthquakes in West Alborz are complicated because their principal stress axes are inconsistent with those derived from the conventional geodetic velocity field. Figure 6 shows the maximum geodetic shear strain directions which should be parallel to one of the nodal planes of the strike-slip systems (Wyss et al. 1992). For the region of 0958, 1608 and 1990 earthquakes, the geodetic shear strain rate directions are oblique to the fault traces.

The comparatively small geodetic strain rate of the region of the 1990 earthquake ($\sim 1.0\text{E}-08 \text{ year}^{-1}$, Fig. 5) is very different from the high seismic strain rate, $\sim 2.3\text{E}-07 \text{ year}^{-1}$. In contrast, the macroseismic areas of the 0958 and 1608 earthquakes have seismic strain rates of $\sim 0.0 \text{ year}^{-1}$. The sharp arrest of the rupture of the 1990 Rudbar earthquake at its southeastern end in addition to frequent microseismic activity in the same region (Tatar and Hatzfeld 2009), even a decade after the earthquake, suggest that the rupture of the 1990 event is incomplete. A number of small and moderate reverse aftershocks, e.g., 1990/06/21 09:02 (5.7), with their

nodal planes perpendicular to the strike of the 1990 faulting at the southeastern end of the 1990 faulting, indicate continued northwestward motion of the unbroken block in Zone 95. The next strike-slip segment marks a 9 km distance to the southeastern end of the 1990 faulting in the form of a compressional step-over and is most likely the reason for the rupture halt (Hu et al. 2016). All these factors indicate the likely maturity of the fault segment to the northwest of Zone 95.

Since short-term slip rates using GPS measurements are inconclusive for the left-lateral system in West Alborz, we prefer to use the long-term estimates for the fault slip rate. Berberian and Walker (2010) considered the left-lateral shear of the overall Alborz belt at a rate of $4 \pm 2 \text{ mm year}^{-1}$. This value matches the left-lateral surface rate for East Alborz which is about 4.5 mm year^{-1} . Nazari et al. (2009), using morphological and paleoseismological methods, estimated minimum horizontal slip rate of $0.6\text{--}1.6 \text{ mm year}^{-1}$ for the Taleghan fault. Based on geological evidence, Guest et al. (2006) estimated a slip velocity of $2.7 \pm 0.5 \text{ mm year}^{-1}$ of long-term left-lateral slip for Taleghan and Moshfa faults located in Zone 95. Assuming a slip rate of about 3.0 mm year^{-1} , the slip deficit for the causative faults of the 0958 and 1608 earthquakes amount to 3.1 and 1.2 m, respectively. A fault system with 3.1 m of slip deficit is mature enough to generate a 7.4 earthquake. There is no reason to consider the macroseismic area of the 0958 earthquake as less mature, compared to the macroseismic area of the 1608 earthquake. As mentioned earlier, this region shows signs of southeastward continuation of the rupture of the 1990 Rudbar earthquake.

The exact location of the left-lateral system in West Alborz is not well known. This also was the case for the causative fault of the 1990 Rudbar earthquake. In most studies the Moshfa fault, which is located about 16 km north of Tehran, is considered to be the continuation of the left-lateral system in West Alborz (e.g., Guest et al. 2006). However, existence of a huge rock-slide, $\sim 1.2 \text{ km} \times 0.25 \text{ km}$, approximately 7 km to the W–NW of Tehran at 35.819250°N , 51.243044°E , suggests that there may be other possibilities for the location of the left-lateral fault system in the vicinity of Tehran.

With a b value of 0.64 and an a / b value of 5.61, Zone 83 is the location of several devastating strike-slip earthquakes along the North Tabriz fault. The most recent major earthquakes of 1721/04/26 (7.7, 63) and 1780/01/08 (7.7, 68) caused widespread devastation with approximately 40,000 and 50,000 deaths, respectively. The relatively high geodetic strain rate in Zone 83 ($\sim 3.2\text{E}\text{--}08 \text{ year}^{-1}$, Fig. 5) is anti-correlated with the relatively small seismic strain rate, $\sim 2.0\text{E}\text{--}10 \text{ year}^{-1}$. The fault-parallel geodetic surface velocity for the region surrounding the North Tabriz fault is $6.23 \pm 1.12 \text{ mm year}^{-1}$, based on our analysis. Therefore, the slip deficit values of less than 2 m since the occurrence of these two earthquakes is much smaller than expected for such major earthquakes. The likely unbroken segments along the North Tabriz fault may be the potential location of future damaging earthquakes. However, we have no clues as to the location of these segments. The low b value of the zone supports this viewpoint but the moderate a / b value suggests maturity of the zone for earthquakes of about 6.5–7. The main segments of the system ruptured during the 1721 and 1780 earthquakes. The unusual feature of these two earthquakes was their largely overlapping surface rupture and the major difference between them was the large normal slip component that reached 4–10 m for the 1780 earthquake in places (Ambraseys and Melville 1982).

5. Conclusion

Simultaneous analysis of geodetic slip rate and slip deficit, geodetic and seismic strain rates, stress drop, G–R distribution and historical and recent seismicity is employed here to identify zones and fault systems in the Iranian Plateau that are favorable candidates for likely future major earthquakes (Fig. 14). However, this does not rule out the occurrence of large earthquakes in other fault systems.

Of the identified faults, F4 is the most important because it passes through a heavily populated area near or in Tehran megacity. Another important segment is F1, which passes next to Baku, the capital of Azerbaijan. F3 is the segment with indications of rupture initiating from its NW tip and propagating southeastward, a continuation of the 1990/06/20 (7.4)

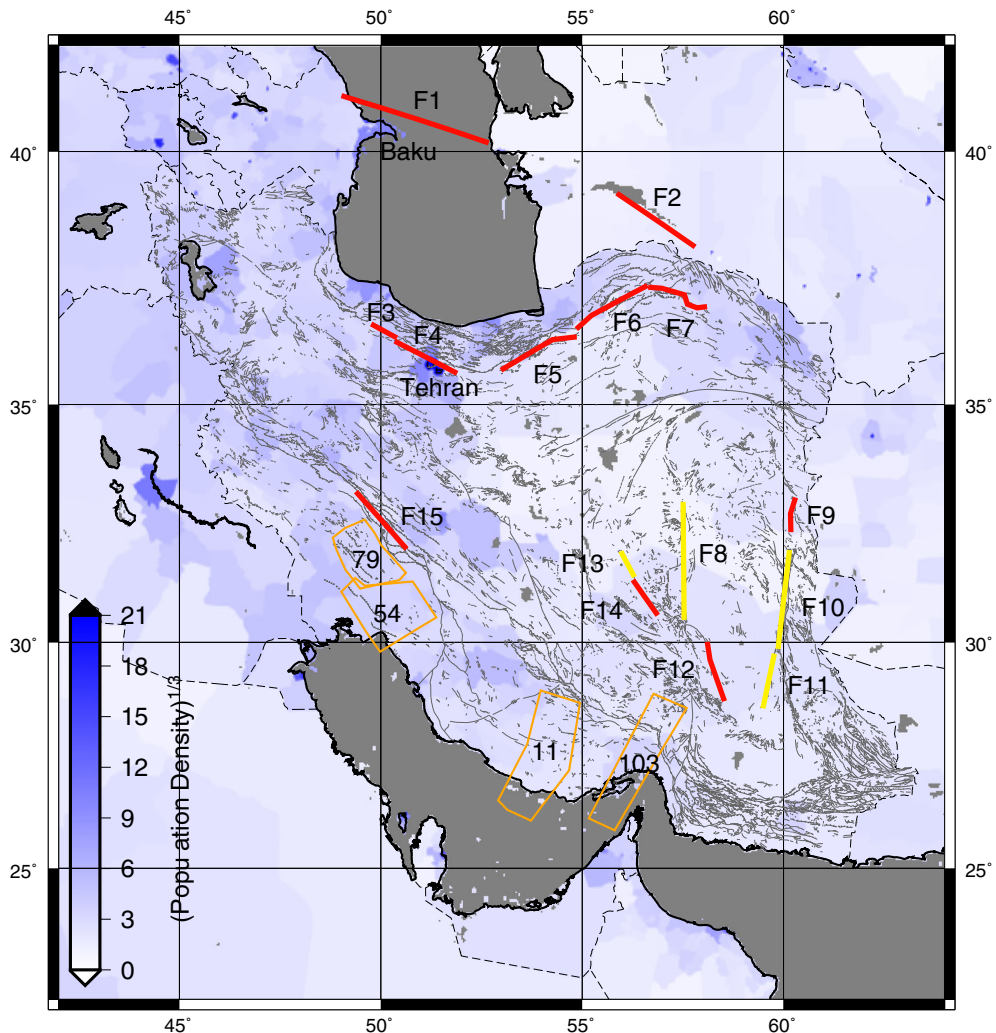


Figure 14

The fault systems which may host future large earthquakes in the Iranian Plateau based on this study. The fault segments in *red* show stronger evidences of maturity compared to those in *yellow*. The four zones of 11, 54, 79 and 103 are in the mature stage of the earthquake cycle. For better rendering, the third root of population density is shown as background

Rudbar faulting. Along the border between the Iranian and the Eurasian plates, F2 is among the most mature fault segments. F6 is part of the system that hosts the 0856 (7.9) earthquake and the associated fault type is likely strike-slip in nature. F7 is expected to be of reverse-type faulting. F9 is the continuation of the 1997/05/10 (7.3) faulting. The four zones of 11, 54, 79 and 103 are identified along the Zagros fold-thrust belt, where blind faulting prevents delineation of the causative faults.

Additional, detailed studies on the fault segments proposed here are necessary. However, the population density along F3 and F4 means that studies in those regions are most imperative. The coupling along F4 seems to be close to 100% and researchers may have been misled by the lack of geodetically-derived differential motion along the fault strike. Therefore denser seismic and geodetic networks and observations are required to better characterize the seismic hazard in the region.

Appendix

See Tables 3 and 4.

Table 3

GPS stations in Iran and Oman, their locations, velocities (mm year⁻¹) and their 1 σ uncertainties with respect to Eurasia-fixed frame (EURA_I08)

Site	Lon.(° E)	Lat.(° N)	V_E	V_N	$1\sigma_{V_E}$	$1\sigma_{V_N}$	R
ABRK	53.2260	31.1200	-1.22	14.21	1.92	1.92	0.00
SBAK	55.1070	30.1460	0.74	13.97	1.35	1.35	0.00
SRCH	55.8850	30.0140	1.33	14.20	1.67	1.66	0.00
GOTR	55.7910	31.4160	0.60	11.54	1.62	1.62	0.00
BRSR	56.7210	29.9970	1.07	15.64	1.69	1.68	0.00
IRAJ	56.4450	30.7750	0.19	13.88	1.60	1.60	0.00
SEND	55.9290	31.7130	0.38	12.69	1.06	1.06	0.00
RAVR	56.8090	31.2520	1.43	11.32	0.76	0.72	0.00
TBAS	56.8190	33.4890	-2.28	8.35	1.59	1.59	0.00
NYBD	57.3970	32.4920	-0.07	9.93	1.26	1.27	0.00
ABJN	57.0460	31.2060	3.31	11.97	1.64	1.64	0.00
KATI	56.3650	31.4130	1.51	11.66	1.08	1.08	0.00
DESL	59.2970	31.1960	2.34	7.53	1.60	1.59	-0.00
KHSF	58.8210	32.7550	0.99	7.05	1.16	1.16	-0.00
ABGR	58.3190	32.4840	1.64	8.29	1.58	1.58	-0.00
NEBA	60.0470	31.5730	1.60	6.60	1.30	1.30	-0.00
ZABL	61.7160	30.8410	2.69	3.04	1.16	0.91	-0.01
HAJT	60.5020	31.5730	1.98	3.00	1.20	1.20	-0.00
BAZ2	60.1770	27.8650	5.50	3.97	1.61	1.59	-0.00
BIJD	59.2550	32.9000	1.41	7.52	0.44	0.35	-0.01
NOGH	59.9370	32.9880	1.72	5.93	1.00	1.01	-0.00
SARB	59.9550	32.5780	1.95	6.22	1.18	1.19	-0.00
HSAD	57.4650	29.3710	3.08	14.94	1.61	1.61	0.00
RAIN	57.5840	29.7620	2.04	14.71	1.59	1.59	0.00
HRMK	57.9170	29.6420	3.25	10.65	1.62	1.60	0.00
BA07	58.3050	29.1490	2.20	12.52	1.48	1.47	0.00
BA13	58.0740	29.2300	2.16	11.61	1.58	1.58	0.00
BA14	57.9400	29.1050	5.75	10.63	1.13	1.12	0.00
BA30	57.9670	29.3160	4.22	10.56	1.13	1.12	0.00
BA31	58.1300	29.1870	3.39	11.71	1.52	1.50	0.00
BA32	58.1410	29.0780	3.56	12.14	1.54	1.52	0.00
BA34	58.2780	28.9440	4.95	10.57	1.62	1.61	0.00
BA35	58.1950	28.8880	5.82	11.59	1.56	1.54	0.00
BA12	58.5230	29.1370	3.89	8.49	1.13	1.12	0.00
BA36	58.4690	28.8980	3.79	9.72	1.49	1.49	0.00
BA38	58.6750	28.9600	6.16	8.31	1.15	1.14	0.00
CMCV	57.7600	30.5370	0.74	9.36	1.64	1.62	0.00
BA09	58.4280	28.7840	6.51	10.78	1.53	1.52	0.00
LALE	56.6900	29.5960	2.12	15.38	1.12	1.12	0.00
BAFT	56.5800	29.2390	1.73	14.31	1.49	1.49	0.00
RAZD	55.8000	28.3300	4.04	15.53	0.99	0.98	0.01
SRJN	55.7070	29.3040	1.12	15.28	1.64	1.63	0.00
SHRZ	52.6030	29.5440	-0.56	14.09	0.57	0.56	-0.02
ABAD	52.5680	31.2280	-0.44	13.73	1.54	1.54	0.00
ABAR	53.3080	31.1230	-0.35	13.10	1.55	1.54	0.00
BAMO	50.9800	30.1090	-1.02	17.98	1.59	1.57	0.00
DASH	51.8140	29.9450	-1.86	15.03	1.57	1.56	-0.00
DAYY	51.8360	27.8500	4.28	19.24	1.68	1.64	-0.01

Table 3
continued

Site	Lon.(° E)	Lat.(° N)	V_E	V_N	$I\sigma_{V_E}$	$I\sigma_{V_N}$	R
MARV	52.7520	29.7980	0.26	13.89	1.56	1.53	-0.00
SEDE	52.1790	30.7260	-0.16	11.79	1.54	1.52	0.00
SEPI	51.3580	30.6100	-2.38	15.87	1.57	1.57	0.00
SHAN	51.7750	28.4000	-0.50	17.91	1.62	1.60	-0.00
YAGH	52.2350	29.6170	-1.41	15.00	1.54	1.53	-0.00
DELO	47.4290	32.6920	-1.49	16.17	1.76	1.75	0.01
GORI	47.7390	33.0570	-3.65	16.68	1.72	1.71	0.01
KORA	48.1750	33.4060	-0.98	16.38	1.68	1.68	0.01
BORU	48.5060	33.7720	-4.63	13.99	1.66	1.66	0.01
DEZF	48.6780	32.6570	-3.94	17.68	1.66	1.65	0.01
AHVA	48.6840	31.3400	-1.49	18.81	1.61	1.61	0.01
AWAZ	48.9250	31.1880	-2.88	20.49	1.68	1.66	0.01
SOLE	49.3280	32.0370	-3.51	18.06	1.65	1.64	0.01
HAFT	49.5710	31.4840	-2.23	21.29	1.66	1.63	0.00
SARD	50.0260	30.3250	-2.43	20.39	1.68	1.66	-0.00
CHEL	50.0980	32.4820	-4.11	17.16	1.64	1.62	0.00
KRD2	50.5310	31.8080	-4.52	15.25	1.62	1.61	0.00
DEDA	50.5780	30.9900	-0.07	17.19	1.64	1.62	0.00
SEMI	51.4300	31.2250	-4.07	13.90	1.63	1.62	-0.00
NOSH	51.7680	36.5860	-4.31	10.44	1.93	1.75	-0.00
KAN2	52.0560	27.8340	0.08	21.94	1.25	1.26	-0.01
FAR2	52.1060	28.8510	-2.70	19.07	1.17	1.15	-0.01
OSL2	52.6070	27.4740	-0.68	22.94	1.89	1.81	-0.00
QIR2	53.0290	28.4770	-2.80	15.37	1.18	1.18	-0.00
ISL2	53.0660	28.3470	-2.06	16.38	1.20	1.20	-0.00
SAA2	53.1460	30.0870	-0.69	12.92	1.17	1.13	-0.00
SVR2	53.2440	29.2810	-2.19	13.94	1.15	1.14	-0.00
BMG2	53.4800	26.9700	2.48	20.37	1.54	1.55	0.00
GOT2	53.6310	28.6240	-1.36	16.27	1.30	1.28	-0.00
BIG2	53.6370	27.8520	-1.23	15.41	1.32	1.32	0.00
TMN2	54.3160	29.2390	-2.44	13.20	1.20	1.20	-0.00
LAR2	54.3200	27.6440	0.05	18.16	1.36	1.36	0.01
DEH2	54.7000	28.6450	-2.63	13.47	1.28	1.27	-0.00
BAGH	55.6570	27.0000	4.84	23.80	2.43	2.25	0.03
FINO	55.8670	27.6510	1.44	19.07	2.33	2.19	0.02
GENO	56.1620	27.3660	4.07	20.98	2.34	2.18	0.02
MINA	57.1000	27.1600	1.55	22.76	2.21	2.05	0.02
MOSH	57.6200	26.9930	1.62	13.73	2.25	2.11	0.02
POOS	57.2370	26.3790	3.04	23.29	2.39	2.22	0.02
SARZ	56.9460	27.4880	-1.27	19.19	2.27	2.12	0.02
SORC	57.8840	27.9010	1.83	13.60	2.24	2.05	0.02
ALIS	51.0820	28.9190	0.66	20.65	1.06	1.03	0.01
BAZM	60.1800	27.8650	5.42	3.74	2.23	1.90	0.02
BAHR	50.6080	26.2090	3.86	20.48	1.33	1.29	-0.01
CHAB	60.6940	25.3000	4.36	8.00	1.82	1.75	0.02
ILAM	46.4270	33.6480	-3.81	16.23	1.10	1.07	0.03
JASK	57.7670	25.6360	2.97	13.16	1.52	1.50	0.02
KHAS	56.2330	26.2080	5.27	25.90	1.37	1.36	0.01
KHOS	48.4090	30.2460	0.02	18.95	1.15	1.10	0.02
LAMB	54.0040	26.8830	2.04	21.19	1.41	1.27	0.00
MUSC	58.5690	23.5640	8.41	26.68	1.94	1.91	0.02
ZABO	61.5170	31.0490	0.92	2.38	1.33	1.23	0.01
BAJE	58.2146	34.5584	-0.45	7.27	0.55	0.54	-0.01
BAKH	60.3602	35.0018	0.91	0.82	0.84	0.82	-0.05

Table 3

continued

Site	Lon.(° E)	Lat.(° N)	V_E	V_N	$I\sigma_{V_E}$	$I\sigma_{V_N}$	R
BIAJ	55.8052	36.0861	1.91	9.31	0.34	0.31	0.00
BIAR	55.9061	35.9884	1.04	9.59	0.59	0.61	-0.01
BOJD	57.2716	37.4803	-1.29	5.59	0.40	0.41	-0.03
DARG	57.5893	35.9148	-0.32	6.28	0.53	0.54	-0.01
DOGH	58.8693	35.1084	0.38	5.46	0.63	0.63	-0.02
ESFA	57.4270	37.1588	0.72	5.06	0.63	0.65	-0.01
ESFN	57.4946	37.0495	1.96	5.83	0.51	0.42	-0.02
FARM	59.8430	35.6961	0.73	2.47	0.60	0.61	-0.07
FERD	58.1831	34.0307	-0.59	8.97	0.49	0.51	0.00
GARD	59.1972	35.4955	-0.30	3.13	0.64	0.64	-0.03
GOLM	59.2478	36.5582	2.09	3.84	0.56	0.53	-0.05
GONA	58.6835	34.3731	-0.00	7.21	0.50	0.47	-0.02
GRME	56.2643	37.0416	-0.73	8.53	0.52	0.53	-0.01
JANA	59.0756	37.4128	-0.37	-0.52	0.69	0.71	-0.03
KADN	58.8783	35.5917	-1.80	2.78	0.62	0.48	-0.03
KALT	59.6404	36.3913	1.23	1.11	0.67	0.60	-0.05
KHAF	60.1103	34.5888	-0.13	1.11	0.79	0.76	-0.04
KHUR	55.0813	33.7693	1.27	11.90	0.39	0.35	-0.02
KSHM	58.4730	35.2706	1.68	5.94	0.42	0.40	-0.03
MAR2	55.9556	37.8445	-4.51	6.31	0.58	0.61	-0.01
MAVT	55.9439	37.8010	-3.93	6.58	0.46	0.37	-0.02
MSHN	59.4798	36.3347	-0.29	1.84	0.55	0.54	-0.06
NFRD	59.4013	36.4501	2.90	5.08	0.59	0.54	-0.05
NISH	58.8203	36.2070	0.17	5.21	0.48	0.49	-0.04
QAE2	59.1877	33.6634	-0.47	5.70	0.74	0.72	-0.00
QAEN	59.1760	33.7400	0.06	6.30	0.65	0.62	-0.01
QUCH	58.5373	37.0707	1.51	2.34	0.51	0.47	-0.03
SABZ	57.6528	36.1849	2.26	7.79	0.38	0.39	-0.02
SAFI	57.9213	36.6981	1.25	5.25	0.55	0.41	-0.02
SARK	61.1486	36.5368	-0.33	0.81	0.87	0.89	-0.07
SHAM	58.4310	37.5699	-0.79	2.74	0.65	0.66	-0.02
SHKH	60.2962	33.6543	0.31	2.07	0.95	0.90	-0.02
TABS	56.9507	33.6034	0.36	10.54	0.50	0.43	0.00
THED	59.2187	35.3469	0.79	4.36	0.51	0.50	-0.05
TJAM	60.5642	35.2944	0.83	3.47	0.79	0.77	-0.07
TORQ	59.6275	36.2241	1.52	0.75	0.59	0.60	-0.06
TOTI	58.5315	33.0192	-0.00	8.97	0.79	0.78	0.01
YAZT	61.0337	36.6013	-0.88	0.03	0.88	0.90	-0.06
ZVNG	58.5147	36.4384	1.86	3.91	0.66	0.67	-0.02
BALA	44.7500	37.5340	-4.04	15.28	0.68	0.69	0.00
GGSH	44.9540	38.2070	2.10	13.52	0.78	0.79	-0.01
HSTD	47.0940	37.5760	-1.55	13.43	0.72	0.72	-0.01
MMKN	44.7710	37.9850	-2.22	10.21	2.46	1.04	-0.00
MNDB	46.0090	36.9300	-5.08	14.89	1.31	0.35	-0.01
SKOH	46.1230	37.9330	-0.64	13.27	0.39	0.62	-0.02
TASJ	45.3610	38.3160	-0.93	13.23	0.39	0.47	-0.03
VLDN	45.1930	38.4920	2.17	14.21	0.44	0.47	-0.03
AHAR	47.0500	38.4680	1.43	9.66	0.32	0.36	-0.05
AMND	46.1550	38.2310	0.99	11.40	0.38	0.33	-0.04
ARBI	48.2310	38.4770	4.15	12.23	0.47	0.46	-0.01
ARDH	47.6500	37.8290	0.83	12.36	0.33	0.44	-0.03
BRMN	47.2880	37.9190	1.15	12.87	0.44	0.30	-0.03
BSOF	45.7320	38.6740	3.41	10.79	0.50	0.40	-0.03
BZGN	44.3920	39.3790	3.54	9.82	0.79	0.80	-0.01

Table 3

continued

Site	Lon.(° E)	Lat.(° N)	V_E	V_N	$I\sigma_{V_E}$	$I\sigma_{V_N}$	R
DAMO	47.7440	39.5130	6.67	14.45	0.49	0.47	-0.03
GOSM	48.4190	38.7060	4.71	12.86	0.95	0.83	-0.00
HEFZ	48.4580	38.0000	3.73	11.97	0.81	0.85	-0.02
JAMI	45.0490	39.2970	4.26	10.16	0.71	0.73	-0.01
JERM	45.6610	39.8370	4.27	11.12	0.97	0.93	-0.02
JOLF	45.6050	38.9520	3.32	11.03	0.70	0.71	-0.01
KBLG	44.5650	39.0310	2.59	12.34	0.90	0.92	-0.01
KHAV	46.2650	38.7360	4.96	9.62	0.68	0.69	-0.01
KHJE	46.5960	38.1520	2.07	10.42	0.76	0.76	-0.01
KLBR	47.0320	38.8690	4.18	12.47	0.75	0.75	-0.01
MOGH	48.0490	39.0130	5.29	11.28	0.82	0.85	-0.02
NORA	46.0930	39.5360	3.53	10.74	1.07	0.96	0.01
NZSF	45.1140	38.9990	3.18	8.70	0.80	0.80	-0.01
ORTA	47.8690	37.9290	3.10	13.58	0.61	0.61	-0.00
PIRM	47.1570	38.9840	4.22	12.06	0.66	0.67	-0.01
POLD	45.0620	39.3510	3.53	10.14	0.48	0.49	-0.03
TAZA	47.2710	38.2700	2.85	11.89	0.59	0.61	-0.01
VARZ	46.6030	38.1780	1.96	12.20	0.53	0.53	-0.02
YARD	48.3880	38.9520	4.92	13.68	0.97	0.89	-0.00
YKKZ	45.4140	38.6720	3.48	10.36	0.62	0.51	-0.02
GHOT	44.4280	38.4890	-2.47	12.10	0.72	0.73	-0.03
ZARI	44.5500	38.4460	-0.58	12.64	0.75	0.76	-0.01
ATTA	50.1000	37.1560	-0.44	13.37	2.10	2.09	0.03
ABAL	51.9860	35.7930	-1.25	10.31	0.52	0.51	0.01
ABAP	51.9870	35.7930	-1.92	9.93	0.58	0.58	-0.00
AMIN	52.5860	35.7010	-2.09	8.56	0.47	0.46	0.01
BLDH	51.8290	36.2080	-2.11	9.71	0.49	0.31	0.00
BOND	50.7320	36.6230	-1.62	11.18	0.74	0.76	0.00
GARM	51.6460	35.9850	-2.27	10.75	0.20	0.36	0.00
GHO1	49.8120	36.6990	-1.64	12.61	0.68	0.71	-0.00
HASH	48.9220	37.7640	2.12	11.59	0.44	0.46	0.00
HELI	52.3050	36.2060	-2.66	10.03	0.58	0.56	0.02
KAHO	53.7390	36.2360	-4.46	5.93	0.71	0.72	0.00
LARZ	52.8110	36.0780	-2.66	8.23	0.68	0.69	0.00
MARG	48.8910	37.1870	-0.45	11.29	0.70	0.72	-0.01
MEHR	52.1570	35.8680	-1.87	8.87	0.52	0.52	0.01
MF02	51.7970	35.8010	-1.12	10.35	0.33	0.33	0.00
MF07	52.0080	35.8970	-0.57	8.72	0.33	0.34	0.00
MF09	51.8330	36.2050	-2.24	10.22	0.36	0.36	0.00
MF10	51.3040	36.3940	-2.72	11.42	0.46	0.47	-0.00
MF12	51.3150	36.1500	-1.32	11.97	0.54	0.54	0.01
MF15	51.6130	35.9880	-2.55	11.60	0.33	0.33	-0.01
PLOR	52.0640	35.8500	-2.47	9.47	0.23	0.29	-0.00
POOL	51.5740	36.4030	-2.51	9.46	0.39	0.33	-0.00
RSHT	49.6240	37.3230	-2.19	13.58	0.17	0.41	-0.00
SHA1	53.4920	36.6790	-4.80	8.30	0.74	0.76	0.01
TN07	51.9940	35.7630	-1.91	9.69	0.47	0.48	0.01
GRGN	54.3530	36.8760	-3.72	6.21	0.61	0.61	0.00
KORD	54.1990	36.8600	-2.50	6.38	0.36	0.34	0.01
MAHM	52.2850	36.5880	-4.04	7.14	0.29	0.26	0.00
NKAD	51.3100	36.6850	-3.92	8.72	0.66	0.49	0.00
SHIR	57.3080	37.8140	-2.99	3.91	0.44	0.41	0.01
TKBN	50.9300	36.7860	-3.40	10.01	0.24	0.26	-0.00
AGKA	48.0050	37.1690	-0.89	12.75	0.53	0.54	0.01

Table 3

continued

Site	Lon.(° E)	Lat.(° N)	V_E	V_N	$I\sigma_{V_E}$	$I\sigma_{V_N}$	R
ARDA	53.8220	32.3130	-1.16	13.84	0.33	0.32	-0.00
BADA	48.8140	36.7640	-0.45	11.37	0.35	0.35	0.00
BES2	54.8320	29.3630	-0.74	14.12	0.41	0.39	0.00
BIJA	47.9300	36.2320	-2.23	13.28	0.35	0.35	0.00
DAND	48.1830	36.6070	0.23	11.82	0.66	0.69	-0.01
DENA	56.5040	28.5290	4.68	14.36	1.04	0.95	-0.02
GHAR	49.8510	35.1400	-2.05	13.40	0.74	0.72	0.00
GHOL	57.2170	28.0100	2.12	15.11	0.98	0.89	-0.01
HAMD	48.5340	34.8690	-2.63	13.54	0.45	0.44	-0.00
HARA	54.6080	30.0790	0.70	13.68	0.41	0.38	-0.00
JOZA	48.9520	34.2560	-3.54	15.56	0.73	0.70	0.00
KERM	57.1190	30.2770	0.47	16.05	0.53	0.45	0.00
KHO2	54.1260	29.9230	-1.27	14.63	0.41	0.39	0.01
KHON	50.4580	33.1570	-2.86	13.23	0.75	0.72	0.01
KHOR	47.1230	37.3680	-2.99	13.18	0.55	0.57	0.01
KRMD	49.2110	36.1960	-2.40	9.75	0.61	0.61	0.00
KSHA	51.2550	34.1500	-2.84	13.04	0.40	0.38	-0.00
MIAN	46.1620	36.9080	-2.43	13.74	0.37	0.35	0.00
QOMS	51.7990	32.2500	-2.61	14.10	0.74	0.70	0.00
SHAB	45.8870	38.2280	1.29	12.19	0.37	0.37	0.01
SHAH	50.7480	32.3670	-2.37	12.84	0.40	0.37	-0.01
SHOL	49.6680	33.0730	-0.80	13.82	0.74	0.71	0.00
TABZ	46.3430	38.0560	-0.88	13.78	0.52	0.53	0.00
TFSH	50.0520	34.6760	-1.71	12.32	0.24	0.24	-0.00
ABSD	52.0910	35.6610	-2.08	8.30	0.14	0.19	-0.00
AKHT	50.6010	35.5880	-1.86	11.64	0.24	0.18	-0.00
ARNG	51.0750	35.9280	-1.78	10.95	0.23	0.21	-0.00
BASH	53.0250	35.7050	0.19	10.32	0.76	0.78	0.00
BOOM	51.8120	35.7300	-1.78	10.57	0.36	0.34	0.00
CHSH	50.9880	35.0880	-1.87	11.08	0.43	0.43	0.00
CHSM	50.9890	35.0880	-1.61	12.07	0.18	0.16	-0.00
DAMA	52.0590	35.7010	-1.78	9.61	0.38	0.38	0.01
FOIM	51.1660	35.4090	-1.68	13.16	0.73	0.74	0.00
FOPM	50.8400	35.7650	-1.75	11.69	0.37	0.20	-0.00
GHAB	54.9890	36.4300	-0.25	10.18	0.71	0.72	0.01
GTCL	51.4100	35.8820	-2.52	11.10	0.55	0.55	0.00
HSGD	50.7470	36.0070	-2.14	11.34	0.18	0.21	-0.00
KASH	58.4640	35.2930	-0.13	5.74	0.34	0.33	-0.00
MF01	51.9550	35.6830	-1.46	9.94	0.42	0.42	-0.00
MF03	51.8850	35.6490	-1.56	10.85	0.32	0.32	-0.00
MF04	52.1170	35.2580	-2.05	11.62	0.36	0.36	0.00
MF05	51.2770	35.4930	-0.82	12.12	0.44	0.43	-0.00
MF06	50.5430	35.2270	-1.20	12.03	0.43	0.43	0.00
MF13	50.6320	36.0090	-1.30	11.45	0.44	0.44	0.00
MF16	51.6650	35.7240	-1.33	11.87	0.33	0.33	-0.00
MF17	51.1080	35.7530	-1.60	10.81	0.32	0.33	-0.00
MOBA	51.8080	34.9770	-0.00	10.66	0.77	0.76	0.04
MOBK	51.7950	35.0530	-1.06	12.21	0.22	0.26	-0.00
NEYA	50.0450	36.4010	-2.45	11.28	0.76	0.80	-0.00
PISH	51.8850	35.2240	-0.87	10.93	0.52	0.51	0.01
PLZI	51.9710	35.6300	-0.71	9.60	0.25	0.31	-0.00
ROBA	56.0700	33.3690	0.65	10.44	0.42	0.39	0.00
RTCL	51.7110	35.5740	-1.36	10.85	0.30	0.19	-0.00
SEMN	53.5640	35.6620	-0.14	8.95	0.42	0.40	0.01

Table 3

continued

Site	Lon.(° E)	Lat.(° N)	V_E	V_N	$I\sigma_{V_E}$	$I\sigma_{V_N}$	R
SHOR	51.8840	35.2770	-0.91	13.23	0.17	0.16	-0.00
SMNN	53.4210	35.5880	0.74	9.61	0.30	0.28	-0.00
TANG	52.0430	35.4920	-0.98	9.94	0.36	0.36	0.01
TEHN	51.3340	35.6970	-1.23	10.86	0.31	0.30	0.00
TEHR	51.3860	35.7470	-0.81	12.87	0.79	0.75	0.01
TF01	51.2570	35.8120	-1.77	12.82	0.42	0.42	0.01
TF09	51.4250	35.8330	-1.42	12.50	0.50	0.50	0.01
TF16	51.5220	35.7740	-1.86	12.30	0.41	0.41	0.01
TF20	51.5680	35.8080	-3.36	11.38	0.51	0.52	0.01
TLGN	50.7450	36.1440	-2.93	11.76	0.48	0.37	-0.00
TN01	51.0000	35.4930	-1.18	13.12	0.70	0.70	0.02
TN02	51.1700	35.2030	-0.80	12.90	0.45	0.46	0.01
TN03	51.3790	35.3660	-0.91	12.77	0.48	0.49	0.01
TN04	51.4090	35.4950	-1.42	13.23	0.46	0.47	0.01
TN05	51.5150	35.6330	-0.46	11.35	0.49	0.50	0.01
TN06	51.7240	35.5500	-0.60	11.25	0.40	0.40	0.01
VRMN	51.6320	35.3440	-0.90	12.66	0.25	0.63	-0.00

R is the correlation coefficient between E and N velocities

Table 4

Geodetic (G) and seismic (S) strain rate axes or magnitude at grid nodes 100 km apart

Lon. (°E)	Lat. (°N)	$\dot{\epsilon}_{max}^G$ (yr ⁻¹)	Trend (°)	$\dot{\epsilon}_{min}^G$ (yr ⁻¹)	Trend (°)	$\dot{\epsilon}_{shear}^G$ (yr ⁻¹)	Trend (°)	$\dot{\epsilon}^S$ (yr ⁻¹)	$\dot{\epsilon}^S / \dot{\epsilon}^G$
57.645	24.056	2.4361E-08	121.27	-1.6108E-07	31.27	1.8544E-07	346.27	0.0000E+00	0.0000E+00
58.620	24.010	9.6990E-09	106.43	-7.4799E-08	16.43	8.4498E-08	331.43	0.0000E+00	0.0000E+00
59.594	23.959	9.5554E-09	105.99	-7.4769E-08	15.99	8.4324E-08	330.99	0.0000E+00	0.0000E+00
57.692	24.953	2.8094E-08	125.09	-1.3070E-07	35.09	1.5879E-07	350.09	0.0000E+00	0.0000E+00
58.675	24.905	1.0567E-08	108.58	-7.1525E-08	18.58	8.2092E-08	333.58	0.0000E+00	0.0000E+00
59.655	24.852	9.7095E-09	106.65	-7.3463E-08	16.65	8.3173E-08	331.65	0.0000E+00	0.0000E+00
60.632	24.791	7.5001E-09	109.20	-6.8785E-08	19.20	7.6285E-08	334.20	0.0000E+00	0.0000E+00
50.766	26.007	-5.0108E-09	35.51	-3.0527E-08	125.51	2.5516E-08	80.51	0.0000E+00	0.0000E+00
51.765	26.005	2.8031E-09	336.63	-7.9796E-09	66.63	1.0783E-08	21.63	0.0000E+00	0.0000E+00
52.764	25.996	1.4775E-08	132.07	-1.7344E-08	42.07	3.2119E-08	357.07	0.0000E+00	0.0000E+00
53.762	25.981	8.0096E-09	108.85	-3.4686E-08	18.85	4.2696E-08	333.85	0.0000E+00	0.0000E+00
54.760	25.958	1.0475E-08	91.62	-3.2715E-08	1.62	4.3190E-08	316.62	0.0000E+00	0.0000E+00
55.756	25.929	-7.3666E-10	117.34	-4.4365E-08	27.34	4.3628E-08	342.34	0.0000E+00	0.0000E+00
56.750	25.893	2.5773E-08	320.34	-5.0246E-08	50.34	7.6019E-08	5.34	5.0944E-11	9.0213E-04
57.742	25.850	4.8581E-08	319.40	-6.5086E-08	49.40	1.1367E-07	4.40	7.4943E-11	9.2275E-04
58.732	25.800	2.7522E-08	318.02	-1.5951E-08	48.02	4.3473E-08	3.02	0.0000E+00	0.0000E+00
59.719	25.744	8.7538E-09	110.35	-2.4724E-08	20.35	3.3478E-08	335.35	1.4492E-09	5.5254E-02
60.703	25.681	6.2660E-09	111.76	-2.6312E-08	21.76	3.2578E-08	336.76	0.0000E+00	0.0000E+00
50.764	26.910	-6.1444E-09	43.68	-2.1521E-08	133.68	1.5377E-08	88.68	0.0000E+00	0.0000E+00
51.771	26.908	-1.1125E-08	4.39	-1.4364E-08	94.39	3.2384E-09	49.39	0.0000E+00	0.0000E+00
52.778	26.899	7.7049E-09	119.05	-4.9276E-08	29.05	5.6981E-08	344.05	0.0000E+00	0.0000E+00
53.784	26.883	1.0477E-08	110.46	-4.1334E-08	20.46	5.1812E-08	335.46	5.6933E-10	1.3352E-02
54.789	26.859	1.3071E-08	96.04	-4.3616E-08	6.04	5.6687E-08	321.04	2.3247E-10	5.1055E-03
55.793	26.829	-2.9504E-09	107.40	-4.7560E-08	17.40	4.4610E-08	332.40	5.9235E-09	1.2431E-01
56.795	26.791	2.0887E-09	125.44	-5.0899E-08	35.44	5.2988E-08	350.44	0.0000E+00	0.0000E+00
57.794	26.747	3.3985E-08	129.20	-5.3077E-08	39.20	8.7062E-08	354.20	6.6718E-09	1.0586E-01
58.792	26.695	3.2033E-08	124.84	-2.4870E-08	34.84	5.6903E-08	349.84	0.0000E+00	0.0000E+00
59.786	26.637	1.4957E-08	110.56	-2.6708E-08	20.56	4.1665E-08	335.56	0.0000E+00	0.0000E+00
60.777	26.571	1.3490E-08	109.36	-2.7353E-08	19.36	4.0843E-08	334.36	1.6604E-09	5.4443E-02

Table 4

continued

Lon. (°E)	Lat. (°N)	$\dot{\epsilon}_{max}^G$ (yr ⁻¹)	Trend (°)	$\dot{\epsilon}_{min}^G$ (yr ⁻¹)	Trend (°)	$\dot{\epsilon}_{shear}^G$ (yr ⁻¹)	Trend (°)	$\dot{\epsilon}^S$ (yr ⁻¹)	$\dot{\epsilon}^S / \dot{\epsilon}^G$
50.762	27.813	4.7453E-10	324.10	-2.0593E-08	54.10	2.1068E-08	9.10	0.0000E+00	0.0000E+00
51.777	27.811	-8.8190E-09	131.94	-4.3066E-08	41.94	3.4247E-08	356.94	4.7236E-11	1.0745E-03
52.792	27.801	1.5685E-09	119.38	-4.6511E-08	29.38	4.8079E-08	344.38	2.0221E-10	4.3451E-03
53.807	27.784	9.5749E-09	109.69	-3.5283E-08	19.69	4.4857E-08	334.69	2.0556E-09	5.6228E-02
54.820	27.760	1.6561E-08	95.09	-3.6916E-08	5.09	5.3477E-08	320.09	3.6738E-09	9.0801E-02
55.832	27.728	2.5957E-09	94.87	-4.3797E-08	4.87	4.6393E-08	319.87	3.4807E-09	7.9333E-02
56.842	27.689	-5.9414E-09	101.30	-3.7761E-08	11.30	3.1819E-08	326.30	3.4381E-08	8.9942E-01
57.849	27.643	1.5159E-08	113.06	-2.6024E-08	23.06	4.1183E-08	338.06	5.3605E-10	1.7799E-02
58.854	27.589	2.0088E-08	116.03	-2.0169E-08	26.03	4.0257E-08	341.03	0.0000E+00	0.0000E+00
59.856	27.529	1.8037E-08	115.18	-2.0065E-08	25.18	3.8102E-08	340.18	0.0000E+00	0.0000E+00
60.855	27.461	1.7015E-08	115.72	-3.6690E-08	25.72	5.3705E-08	340.72	2.8219E-10	6.9773E-03
50.760	28.715	5.6555E-09	133.35	-3.9983E-08	43.35	4.5639E-08	358.35	0.0000E+00	0.0000E+00
51.784	28.713	2.6966E-10	127.65	-3.5133E-08	37.65	3.5402E-08	352.65	7.0124E-09	1.9959E-01
52.807	28.703	-1.3116E-09	117.30	-2.8568E-08	27.30	2.7257E-08	342.30	1.6458E-08	5.7549E-01
53.830	28.686	3.8949E-09	102.97	-1.7854E-08	12.97	2.1749E-08	327.97	0.0000E+00	0.0000E+00
54.852	28.661	1.9687E-08	92.03	-1.6544E-08	2.03	3.6231E-08	317.03	2.9378E-09	1.1424E-01
55.872	28.628	1.5882E-08	95.65	-1.8568E-08	5.65	3.4451E-08	320.65	1.3635E-08	5.5802E-01
56.891	28.587	8.8665E-09	108.35	-1.8887E-08	18.35	2.7753E-08	333.35	4.1623E-09	1.9949E-01
57.907	28.539	2.1552E-08	113.14	-1.8912E-08	23.14	4.0464E-08	338.14	1.6511E-08	5.7583E-01
58.920	28.484	2.3717E-08	118.06	-2.2751E-08	28.06	4.6468E-08	343.06	4.8127E-11	1.4644E-03
59.930	28.421	1.8600E-08	120.50	-2.9440E-08	30.50	4.8040E-08	345.50	1.6442E-08	4.7216E-01
60.937	28.350	2.0490E-08	318.90	-1.8676E-08	48.90	3.9166E-08	3.90	0.0000E+00	0.0000E+00
48.693	29.598	5.3457E-09	345.01	-1.2570E-08	75.01	1.7915E-08	30.01	0.0000E+00	0.0000E+00
49.725	29.612	4.6544E-09	126.18	-1.8022E-08	36.18	2.2677E-08	351.18	0.0000E+00	0.0000E+00
50.758	29.618	1.0637E-08	122.53	-3.4854E-08	32.53	4.5492E-08	347.53	2.9920E-10	8.2105E-03
51.791	29.616	7.0527E-09	116.48	-2.8838E-08	26.48	3.5891E-08	341.48	6.2599E-09	2.1086E-01
52.823	29.606	2.7560E-10	99.40	-1.6794E-08	9.40	1.7069E-08	324.40	2.5123E-09	1.4958E-01
53.855	29.587	3.4423E-09	71.51	-9.1362E-09	341.51	1.2578E-08	296.51	0.0000E+00	0.0000E+00
54.886	29.561	1.5635E-08	73.68	-5.1618E-09	343.68	2.0797E-08	298.68	0.0000E+00	0.0000E+00
55.915	29.527	1.2325E-08	100.86	-4.4198E-09	10.86	1.6745E-08	325.86	0.0000E+00	0.0000E+00
56.942	29.485	2.1729E-08	126.53	-1.1517E-08	36.53	3.3246E-08	351.53	1.5420E-08	6.2701E-01
57.967	29.435	2.8636E-08	125.10	-2.5351E-08	35.10	5.3987E-08	350.10	1.7669E-08	4.6199E-01
58.989	29.378	3.1987E-08	125.58	-3.4361E-08	35.58	6.6349E-08	350.58	1.4621E-08	3.1146E-01
60.007	29.312	2.3118E-08	134.99	-2.1775E-08	44.99	4.4894E-08	359.99	4.5736E-10	1.4401E-02
61.023	29.239	2.0739E-08	319.98	-1.6572E-08	49.98	3.7311E-08	4.98	0.0000E+00	0.0000E+00
48.672	30.500	2.9103E-09	342.50	-1.0501E-08	72.50	1.3412E-08	27.50	0.0000E+00	0.0000E+00
49.714	30.514	6.5229E-09	125.77	-1.5943E-08	35.77	2.2466E-08	350.77	2.5727E-10	1.4935E-02
50.756	30.520	1.1861E-08	122.66	-3.0627E-08	32.66	4.2488E-08	347.66	3.5134E-09	1.0698E-01
51.798	30.518	1.2897E-08	115.85	-1.8203E-08	25.85	3.1100E-08	340.85	3.7308E-09	1.6723E-01
52.840	30.508	4.2684E-09	100.95	-5.5487E-09	10.95	9.8170E-09	325.95	0.0000E+00	0.0000E+00
53.881	30.489	5.4823E-09	73.23	-3.4356E-09	343.23	8.9179E-09	298.23	0.0000E+00	0.0000E+00
54.921	30.462	8.0175E-09	83.94	-8.6880E-09	353.94	1.6705E-08	308.94	0.0000E+00	0.0000E+00
55.959	30.426	6.0982E-09	89.30	-1.3508E-08	359.30	1.9606E-08	314.30	0.0000E+00	0.0000E+00
56.996	30.383	1.2798E-08	113.30	-2.0110E-08	23.30	3.2907E-08	338.30	9.3466E-09	3.9211E-01
58.030	30.331	2.2966E-08	121.62	-2.9092E-08	31.62	5.2058E-08	346.62	0.0000E+00	0.0000E+00
59.060	30.271	2.4700E-08	123.39	-1.8192E-08	33.39	4.2892E-08	348.39	0.0000E+00	0.0000E+00
60.088	30.203	1.3776E-08	131.63	-1.8372E-08	41.63	3.2148E-08	356.63	1.0720E-08	4.6684E-01
61.112	30.128	1.0669E-08	128.01	-2.0600E-08	38.01	3.1269E-08	353.01	0.0000E+00	0.0000E+00
48.650	31.401	-5.4494E-09	113.79	-1.3767E-08	23.79	8.3173E-09	338.79	0.0000E+00	0.0000E+00
49.701	31.416	8.6811E-09	122.69	-2.5724E-08	32.69	3.4405E-08	347.69	1.7651E-10	6.5014E-03
50.753	31.423	1.2094E-08	124.20	-2.9688E-08	34.20	4.1783E-08	349.20	2.4348E-09	7.5954E-02
51.806	31.420	1.4524E-08	115.85	-1.0432E-08	25.85	2.4956E-08	340.85	1.2057E-10	6.7424E-03
52.857	31.410	8.9568E-09	115.02	4.4658E-10	25.02	8.5102E-09	340.02	0.0000E+00	0.0000E+00
53.908	31.390	5.0872E-09	111.89	-1.0600E-09	21.89	6.1472E-09	336.89	0.0000E+00	0.0000E+00
54.958	31.362	7.6828E-09	103.63	-7.9396E-09	13.63	1.5622E-08	328.63	0.0000E+00	0.0000E+00

Table 4

continued

Lon. (°E)	Lat. (°N)	$\dot{\epsilon}_{max}^G$ (yr ⁻¹)	Trend (°)	$\dot{\epsilon}_{min}^G$ (yr ⁻¹)	Trend (°)	$\dot{\epsilon}_{shear}^G$ (yr ⁻¹)	Trend (°)	$\dot{\epsilon}^S$ (yr ⁻¹)	$\dot{\epsilon}^S / \dot{\epsilon}^G$
56.006	31.325	8.9729E-09	93.86	-1.5352E-08	3.86	2.4325E-08	318.86	2.3983E-10	1.3487E-02
57.052	31.280	7.3725E-09	104.60	-1.9513E-08	14.60	2.6885E-08	329.60	1.5859E-09	7.6027E-02
58.095	31.226	8.7010E-09	119.95	-1.6567E-08	29.95	2.5268E-08	344.95	0.0000E+00	0.0000E+00
59.136	31.164	1.1470E-08	125.79	-1.4533E-08	35.79	2.6003E-08	350.79	2.0883E-10	1.1279E-02
60.173	31.094	1.0242E-08	130.44	-1.9421E-08	40.44	2.9663E-08	355.44	1.0062E-10	4.5827E-03
61.206	31.016	6.7194E-09	120.33	-3.7935E-08	30.33	4.4655E-08	345.33	0.0000E+00	0.0000E+00
47.566	32.278	-9.4936E-09	109.78	-1.1959E-08	19.78	2.4652E-09	334.78	1.0603E-08	6.9439E-01
48.627	32.303	-2.4845E-09	103.51	-2.1124E-08	13.51	1.8640E-08	328.51	4.4795E-09	2.1061E-01
49.689	32.318	2.2083E-09	110.50	-2.7003E-08	20.50	2.9211E-08	335.50	4.5767E-09	1.6892E-01
50.751	32.325	6.8160E-09	114.03	-2.1573E-08	24.03	2.8389E-08	339.03	0.0000E+00	0.0000E+00
51.813	32.322	8.8933E-09	103.22	-5.7720E-09	13.22	1.4665E-08	328.22	0.0000E+00	0.0000E+00
52.876	32.311	9.8137E-09	116.71	1.2637E-10	26.71	9.6873E-09	341.71	0.0000E+00	0.0000E+00
53.937	32.291	9.8104E-09	120.64	-1.0697E-09	30.64	1.0880E-08	345.64	0.0000E+00	0.0000E+00
54.997	32.262	8.8482E-09	108.39	-6.8277E-09	18.39	1.5676E-08	333.39	0.0000E+00	0.0000E+00
56.055	32.224	7.2663E-09	115.26	-1.2466E-08	25.26	1.9733E-08	340.26	4.4957E-11	3.1157E-03
57.111	32.177	1.1251E-08	117.16	-1.5074E-08	27.16	2.6325E-08	342.16	0.0000E+00	0.0000E+00
58.164	32.122	1.3678E-08	122.62	-1.3461E-08	32.62	2.7138E-08	347.62	0.0000E+00	0.0000E+00
59.214	32.057	1.1723E-08	126.04	-1.2267E-08	36.04	2.3991E-08	351.04	1.2723E-09	7.4980E-02
60.261	31.985	1.3038E-08	130.34	-1.7567E-08	40.34	3.0605E-08	355.34	1.0062E-10	4.5994E-03
61.303	31.904	8.4918E-09	132.47	-1.5649E-08	42.47	2.4141E-08	357.47	0.0000E+00	0.0000E+00
46.462	33.144	7.6138E-09	127.53	-9.1513E-09	37.53	1.6765E-08	352.53	5.3173E-10	4.4666E-02
47.532	33.179	7.8704E-10	108.51	-1.2977E-08	18.51	1.3765E-08	333.51	5.0198E-10	3.8611E-02
48.603	33.204	1.2509E-09	105.30	-1.7286E-08	15.30	1.8537E-08	330.30	3.0417E-09	1.7551E-01
49.675	33.220	4.0533E-09	106.18	-1.7158E-08	16.18	2.1211E-08	331.18	1.6218E-07	9.1990E+00
50.748	33.227	-2.9420E-10	112.89	-9.3396E-09	22.89	9.0454E-09	337.89	0.0000E+00	0.0000E+00
51.822	33.224	4.6850E-09	90.69	-6.3683E-09	0.69	1.1053E-08	315.69	0.0000E+00	0.0000E+00
52.895	33.213	7.8739E-09	86.66	-7.2898E-09	356.66	1.5164E-08	311.66	0.0000E+00	0.0000E+00
53.967	33.192	7.8212E-09	88.98	-7.3369E-09	358.98	1.5158E-08	313.98	0.0000E+00	0.0000E+00
55.037	33.162	6.4934E-10	122.30	-7.3369E-09	32.30	7.9862E-09	347.30	0.0000E+00	0.0000E+00
56.106	33.122	7.4075E-11	317.45	-1.7097E-08	47.45	1.7171E-08	2.45	8.4314E-11	4.9315E-03
57.172	33.074	8.2760E-09	120.09	-1.1279E-08	30.09	1.9555E-08	345.09	2.1602E-07	1.5442E+01
58.236	33.017	1.3880E-08	121.61	-1.3050E-08	31.61	2.6929E-08	346.61	1.7776E-08	9.3305E-01
59.296	32.950	1.5286E-08	120.07	-1.9736E-08	30.07	3.5022E-08	345.07	1.2723E-09	5.0965E-02
60.353	32.875	1.5129E-08	121.76	-2.6599E-08	31.76	4.1728E-08	346.76	0.0000E+00	0.0000E+00
61.406	32.791	1.3009E-08	129.13	-3.4876E-08	39.13	4.7885E-08	354.13	0.0000E+00	0.0000E+00
46.414	34.044	7.8180E-09	109.69	-1.1901E-08	19.69	1.9719E-08	334.69	3.4209E-11	2.4025E-03
47.495	34.079	3.8035E-09	106.08	-1.2944E-08	16.08	1.6748E-08	331.08	1.6501E-08	1.2231E+00
48.578	34.105	4.5495E-09	105.84	-1.0614E-08	15.84	1.5164E-08	330.84	1.8022E-09	1.5607E-01
49.661	34.122	8.0661E-09	107.30	-7.3127E-09	17.30	1.5379E-08	332.30	0.0000E+00	0.0000E+00
50.746	34.129	2.0912E-09	96.64	-5.8866E-09	6.64	7.9778E-09	321.64	4.4215E-09	7.0778E-01
51.830	34.126	5.0616E-09	107.27	-8.1773E-09	17.27	1.3239E-08	332.27	0.0000E+00	0.0000E+00
52.914	34.114	8.0426E-09	102.28	-1.3969E-08	12.28	2.2012E-08	327.28	1.6408E-09	1.0179E-01
53.998	34.093	8.9374E-09	94.88	-1.4782E-08	4.88	2.3719E-08	319.88	0.0000E+00	0.0000E+00
55.079	34.061	-1.0138E-09	129.41	-1.6850E-08	39.41	1.5836E-08	354.41	0.0000E+00	0.0000E+00
56.159	34.021	-9.0055E-10	335.30	-1.1913E-08	65.30	1.1013E-08	20.30	0.0000E+00	0.0000E+00
57.237	33.971	3.4869E-09	112.17	-9.8693E-09	22.17	1.3356E-08	337.17	2.1602E-07	2.0638E+01
58.311	33.911	1.0258E-08	118.08	-1.5624E-08	28.08	2.5882E-08	343.08	1.7776E-08	9.5106E-01
59.382	33.843	1.4434E-08	120.32	-2.4750E-08	30.32	3.9184E-08	345.32	2.0716E-07	7.2305E+00
60.450	33.765	1.5585E-08	120.12	-2.7404E-08	30.12	4.2989E-08	345.12	1.6509E-09	5.2366E-02
61.513	33.678	1.4710E-08	123.86	-2.7713E-08	33.86	4.2423E-08	348.86	0.0000E+00	0.0000E+00
46.365	34.942	6.8491E-09	103.79	-7.2862E-09	13.79	1.4135E-08	328.79	3.4209E-11	3.4210E-03
47.457	34.979	1.3997E-09	95.85	-9.1811E-09	5.85	1.0581E-08	320.85	1.6501E-08	1.7767E+00
48.551	35.006	3.2439E-09	88.76	-1.2066E-08	358.76	1.5310E-08	313.76	1.2968E-10	1.0379E-02
49.647	35.023	5.3981E-09	97.70	-1.0213E-08	7.70	1.5611E-08	322.70	2.7593E-08	2.3886E+00
50.743	35.031	6.4983E-09	112.99	-1.0629E-08	22.99	1.7128E-08	337.99	0.0000E+00	0.0000E+00

Table 4
continued

Lon. (°E)	Lat. (°N)	$\dot{\epsilon}_{max}^G$ (yr^{-1})	Trend (°)	$\dot{\epsilon}_{min}^G$ (yr^{-1})	Trend (°)	$\dot{\epsilon}_{shear}^G$ (yr^{-1})	Trend (°)	$\dot{\epsilon}^S$ (yr^{-1})	$\dot{\epsilon}^S / \dot{\epsilon}^G$
51.839	35.028	9.9699E-09	119.85	-1.9032E-08	29.85	2.9002E-08	344.85	0.0000E+00	0.0000E+00
52.935	35.016	1.3112E-08	114.32	-2.3595E-08	24.32	3.6707E-08	339.32	1.8783E-09	6.9583E-02
54.030	34.993	9.8841E-09	110.44	-2.1784E-08	20.44	3.1668E-08	335.44	0.0000E+00	0.0000E+00
55.123	34.961	7.4072E-09	91.19	-8.6216E-09	1.19	1.6029E-08	316.19	0.0000E+00	0.0000E+00
56.215	34.919	-2.0043E-11	127.90	-1.0673E-08	37.90	1.0653E-08	352.90	0.0000E+00	0.0000E+00
57.304	34.867	1.1538E-09	114.70	-1.3772E-08	24.70	1.4926E-08	339.70	1.6419E-09	1.1880E-01
58.390	34.806	6.4018E-09	117.13	-2.0691E-08	27.13	2.7092E-08	342.13	1.6496E-07	7.6165E+00
59.472	34.735	1.0067E-08	119.83	-1.9578E-08	29.83	2.9645E-08	344.83	2.6406E-09	1.1995E-01
60.550	34.654	1.0164E-08	123.87	-1.1214E-08	33.87	2.1378E-08	348.87	0.0000E+00	0.0000E+00
61.624	34.565	4.5319E-09	112.59	-4.7054E-10	22.59	5.0025E-09	337.59	0.0000E+00	0.0000E+00
46.313	35.841	1.6591E-08	89.87	-6.6783E-09	359.87	2.3270E-08	314.87	3.6781E-11	2.0566E-03
47.418	35.879	1.2906E-08	93.69	-7.3825E-09	3.69	2.0289E-08	318.69	0.0000E+00	0.0000E+00
48.524	35.907	-5.3968E-10	84.68	-6.8993E-09	354.68	6.3596E-09	309.68	1.2968E-10	1.8739E-02
49.632	35.925	-6.0498E-11	102.56	-6.2823E-09	12.56	6.2218E-09	327.56	2.7593E-08	4.3920E+00
50.740	35.932	5.8213E-09	120.74	-1.7613E-08	30.74	2.3435E-08	345.74	0.0000E+00	0.0000E+00
51.849	35.930	1.1552E-08	123.49	-2.6069E-08	33.49	3.7621E-08	348.49	0.0000E+00	0.0000E+00
52.957	35.917	1.5130E-08	121.35	-2.6525E-08	31.35	4.1655E-08	346.35	1.8783E-09	6.1509E-02
54.064	35.894	2.0331E-08	113.80	-2.7037E-08	23.80	4.7368E-08	338.80	1.9100E-09	5.6461E-02
55.170	35.860	1.8566E-08	105.18	-1.7292E-08	15.18	3.5857E-08	330.18	0.0000E+00	0.0000E+00
56.273	35.817	8.2579E-09	121.11	-1.7486E-08	31.11	2.5744E-08	346.11	0.0000E+00	0.0000E+00
57.374	35.763	3.2825E-09	118.96	-1.5525E-08	28.96	1.8808E-08	343.96	3.9034E-10	2.4599E-02
58.472	35.700	4.0211E-09	119.70	-1.6361E-08	29.70	2.0382E-08	344.70	1.9018E-09	1.1288E-01
59.566	35.626	5.7888E-09	116.50	-1.3208E-08	26.50	1.8997E-08	341.50	3.4446E-10	2.3886E-02
60.656	35.543	2.8000E-09	128.69	-1.0356E-08	38.69	1.3156E-08	353.69	1.1346E-10	1.0576E-02
61.741	35.451	-5.8957E-10	131.32	-1.1636E-08	41.32	1.1047E-08	356.32	4.6020E-10	3.9499E-02
46.259	36.740	1.8191E-08	71.59	-1.4728E-08	341.59	3.2919E-08	296.59	0.0000E+00	0.0000E+00
47.376	36.779	1.8323E-08	74.95	-5.6415E-09	344.95	2.3965E-08	299.95	0.0000E+00	0.0000E+00
48.495	36.808	8.3895E-09	40.07	-4.8645E-09	130.07	1.3254E-08	85.07	0.0000E+00	0.0000E+00
49.616	36.826	7.7313E-09	15.73	-6.1905E-09	105.73	1.3922E-08	60.73	2.3273E-07	2.3498E+01
50.737	36.834	3.2144E-09	133.37	-2.0529E-08	43.37	2.3744E-08	358.37	0.0000E+00	0.0000E+00
51.859	36.831	9.2643E-09	127.26	-2.9189E-08	37.26	3.8453E-08	352.26	6.1447E-09	2.0065E-01
52.980	36.818	1.4111E-08	124.77	-2.4579E-08	34.77	3.8689E-08	349.77	1.7057E-08	6.0185E-01
54.099	36.794	1.9300E-08	108.83	-2.4759E-08	18.83	4.4059E-08	333.83	2.8597E-09	9.1093E-02
55.218	36.759	2.0504E-08	104.35	-2.1900E-08	14.35	4.2404E-08	329.35	0.0000E+00	0.0000E+00
56.334	36.714	2.0130E-08	116.99	-2.3373E-08	26.99	4.3503E-08	341.99	0.0000E+00	0.0000E+00
57.447	36.659	1.2135E-08	117.11	-2.4167E-08	27.11	3.6301E-08	342.11	0.0000E+00	0.0000E+00
58.557	36.594	6.4183E-09	115.40	-2.1795E-08	25.40	2.8213E-08	340.40	1.6445E-10	7.2382E-03
59.664	36.518	1.7325E-09	119.04	-1.6458E-08	29.04	1.8190E-08	344.04	0.0000E+00	0.0000E+00
60.766	36.432	-2.5021E-09	316.05	-1.6588E-08	46.05	1.4086E-08	1.05	0.0000E+00	0.0000E+00
45.074	37.586	2.4556E-08	69.30	-2.4304E-08	339.30	4.8860E-08	294.30	1.1868E-09	3.4350E-02
46.202	37.638	1.9720E-08	66.89	-2.3782E-08	336.89	4.3502E-08	291.89	0.0000E+00	0.0000E+00
47.333	37.678	2.3486E-08	64.12	-1.6434E-08	334.12	3.9920E-08	289.12	2.7829E-10	9.7084E-03
48.465	37.708	1.8911E-08	52.68	-9.9352E-09	322.68	2.8846E-08	277.68	6.4729E-09	3.0301E-01
49.599	37.727	1.4116E-08	32.71	-1.4914E-08	122.71	2.9030E-08	77.71	1.1849E-10	5.7699E-03
56.398	37.612	2.8243E-08	116.90	-3.1193E-08	26.90	5.9437E-08	341.90	0.0000E+00	0.0000E+00
57.524	37.555	2.3723E-08	119.27	-3.6354E-08	29.27	6.0077E-08	344.27	2.5112E-08	5.7849E-01
58.647	37.487	1.3910E-08	118.91	-3.7728E-08	28.91	5.1639E-08	343.91	1.7044E-08	4.2387E-01
59.766	37.409	3.7177E-09	119.24	-3.4608E-08	29.24	3.8326E-08	344.24	6.0829E-10	1.7476E-02
45.001	38.483	2.4457E-08	71.78	-2.3691E-08	341.78	4.8148E-08	296.78	1.2939E-10	3.8000E-03
46.143	38.536	1.7992E-08	66.55	-2.2303E-08	336.55	4.0295E-08	291.55	1.7482E-08	6.1006E-01
47.287	38.578	2.2642E-08	57.83	-1.6351E-08	327.83	3.8994E-08	282.83	0.0000E+00	0.0000E+00
48.434	38.609	2.3333E-08	52.52	-9.2946E-09	322.52	3.2627E-08	277.52	3.4134E-09	1.3590E-01
49.582	38.628	1.8190E-08	36.18	-1.6415E-08	126.18	3.4605E-08	81.18	5.0032E-10	2.0420E-02
44.925	39.379	1.6982E-08	70.37	-1.8240E-08	340.37	3.5222E-08	295.37	7.2905E-08	2.9254E+00
46.081	39.434	1.4599E-08	61.24	-1.2236E-08	331.24	2.6834E-08	286.24	1.7524E-09	9.1995E-02

Table 4

continued

Lon. (°E)	Lat. (°N)	$\dot{\epsilon}_{max}^G$ (yr ⁻¹)	Trend (°)	$\dot{\epsilon}_{min}^G$ (yr ⁻¹)	Trend (°)	$\dot{\epsilon}_{shear}^G$ (yr ⁻¹)	Trend (°)	$\dot{\epsilon}^S$ (yr ⁻¹)	$\dot{\epsilon}^S / \dot{\epsilon}^G$
47.240	39.477	2.5844E-08	49.91	-8.5443E-09	319.91	3.4388E-08	274.91	0.0000E+00	0.0000E+00
48.401	39.509	2.9884E-08	43.41	-5.5440E-09	133.41	3.5428E-08	88.41	0.0000E+00	0.0000E+00

The trend of each strain axis is given in the next column. Columns 3, 5 and 7 are the maximum, minimum and shear geodetic strain rate respectively. Column 9 is the seismic strain rate and the last column is the ratio of the seismic to geodetic strain rate

REFERENCES

- Adeli, H. (1982). The Sirch (Kerman, Iran) Earthquake of 28 July 1981—A field investigation. *Bulletin of the Seismological Society of America*, 72, 841–861.
- Ahmadi, G., Mostaghel, N., & Nowroozi, A. A. (1989). Probabilistic seismic risk for various peak ground accelerations. *Iranian Journal of Science and Technology*, 13, 115–156.
- Allmann, B. P., & Shearer, P. M. (2009). Global variations of stress drop for moderate to large earthquakes. *Journal of Geophysical Research*, 114(B1), B01310.
- Allmendinger, R. W., Reilinger, R., & Loveless, J. (2007). Strain and rotation rate from GPS in Tibet, Anatolia, and the Altiplano. *Tectonics*, 26, TC3013. doi:10.1029/2006TC002.030.
- Altamimi, Z., Métivier, L., & Collilieux, X. (2012). ITRF2008 plate motion model. *Journal of Geophysical Research*. doi:10.1029/2011JB008930.
- Ambraseys, N., & Melville, C. (1982). *A History of Persian Earthquakes*, 219 pp., Cambridge University Press, Cambridge.
- Ambraseys, N. N. (1977). The Seismicity of Kuhistan. *Iran, The Geographical Journal*, 143. doi:10.2307/1795.872.
- Ambraseys, N. N. (1997). The Krasnovodsk (Turkmenistan) earthquake of 8 July 1895. *Journal of Earthquake Engineering*, 01(02), 293–317. doi:10.1142/S1363246997000131.
- Amitrano, D. (2003). Brittle-ductile transition and associated seismicity: Experimental and numerical studies and relationship with the b value. *Journal of Geophysical Research*, 108(B1).
- Amorése, D. (2007). Applying a change-point detection method on frequency-magnitude distributions. *Bulletin of the Seismological Society of America*, 97(5), 1742–1749. doi:10.1785/0120060181.
- Authemayou, C., Bellier, O., Chardon, D., Benedetti, L., Malenkzade, Z., Claude, C., et al. (2009). Quaternary slip-rates of the Kazerun and the Main Recent Faults: active strike-slip partitioning in the Zagros fold-and-thrust belt. *Geophysical Journal International*, 178(1), 524–540. doi:10.1111/j.1365-246X.2009.04191.x.
- Bahroudi, A., & Koyi, H. (2003). Effect of spatial distribution of Hormuz salt on deformation style in the Zagros fold and thrust belt: an analogue modelling approach. *Journal of the Geological Society*, 160(5), 719–733.
- Bak, P., & Tang, C. (1989). Earthquakes as a self-organized critical phenomenon. *Journal of Geophysical Research*, 94(15), 15635–15637.
- Berberian, M. (1976). Contribution to the Seismotectonics of Iran, Part II, Report 39, *Tech. rep.*, Geol. Surv. Iran.
- Berberian, M. (1995). Master “blind” thrust faults hidden under the Zagros folds: active basement tectonics and surface morphotectonics. *Tectonophysics*, 241(3), 193–224.
- Berberian, M., & King, G. C. P. (1981). Towards a palaeogeography and tectonic evolution of Iran. *Canadian Journal of Earth Sciences*, 18, 210–265.
- Berberian, M., & Walker, R. (2010). seismotectonics, coseismic and geomorphic displacements, and historic earthquakes of the western ‘High-Alborz’, Iran. *Geophysical Journal International*, 182(3), 1577–1602. doi:10.1111/j.1365-246X.2010.04705.x.
- Berberian, M., Asudeh, I., & Arshadi, S. (1979). Surface rupture and mechanism of the Bob-Tangol (southeastern Iran) earthquake of 19 December 1977. *Earth and Planetary Science Letters*, 42(3), 456–462. doi:10.1016/0012-821X(79)90055-4.
- Berberian, M., Qorashi, M., Jackson, J., Priestley, K., & Wallace, T. (1992). The Rudbar-Tarom earthquake of 20 June 1990 in NW Persia: Preliminary field and seismological observations, and its tectonic significance. *Bulletin of the Seismological Society of America*, 82(4), 1726–1755.
- Bilham, R. (2009). The seismic future of cities. *Bulletin of Earthquake Engineering*. doi:10.1007/s10518-009-9147-0.
- Brown, L., Wang, K., & Sun, T. (2015). Static stress drop in the Mw 9 Tohoku-oki earthquake: Heterogeneous distribution and low average value. *Geophysical Research Letters*, 42(24), 10595–10600. doi:10.1002/2015GL066361.
- Brune, J. N. (1970). Tectonic stress and the spectra of seismic shear waves from earthquakes. *Journal of Geophysical Research*, 75(26), 4997–5009.
- Cardozo, N., & Allemandigner, R. W. (2009). SSPX: A program to compute strain from displacement/velocity data. *Computational GeoSciences*, 35, 1343–1357.
- Djamour, Y., Vernant, P., Bayer, R., Nankali, H. R., Ritz, J.-F., Hinderer, J., et al. (2010). GPS and gravity constraints on continental deformation in the Alborz mountain range, Iran. *Geophysical Journal International*, 183(3), 1287–1301.
- Dogan, B., & Karakas, A. (2013). Geometry of co-seismic surface ruptures and tectonic meaning of the 23 October 2011 Mw 7.1 Van earthquake (East Anatolian Region, Turkey). *Journal of Structural Geology*, 46, 99–114. doi:10.1016/j.jsg.2012.10.001.
- Dziewonski, A. M., & Anderson, D. L. (1981). Preliminary reference Earth model. *Physics of the Earth and Planetary Interiors*, 25(4), 297–356.
- Ekström, G., Nettles, M., & Dziewonski, A. M. (2012). The global CMT project 2004–2010: Centroid-moment tensors for 13,017 earthquakes. *Physics of the Earth and Planetary Interiors*, 200, 1–9. doi:10.1016/j.pepi.2012.04.002.
- Engdahl, E. R., Jackson, J. A., Myers, S. C., Bergman, E. A., & Priestley, K. (2006). Relocation and assessment of seismicity in the Iran region. *Geophysical Journal International*, 167(2), 761–778. doi:10.1111/j.1365-246X.2006.03127.x.

- Falcon, N. L. (1974). Southern Iran: Zagros mountains, in Mesozoic-Cenozoic Orogenic Belts. *Geological Society of London Special Publication*, 4, 199–211.
- Frohlich, C. (2006). *Deep Earthquakes*. Cambridge, United Kingdom, Cambridge University Press, p. 592.
- Gao, L., & Wallace, T. C. (1995). The 1990 Rudbar-Tarom Iranian earthquake sequence: Evidence for slip partitioning. *Journal of Geophysical Research*, 100(B8), 15317–15332.
- Gardner, J. K., & Knopoff, L. (1974). Is the sequence of earthquakes in Southern California, with aftershocks removed, Poissonian? *Bulletin of the Seismological Society of America*, 64(5), 1363–1367.
- Guest, B., Axen, G. J., Lam, P. S., & Hassanzadeh, J. (2006). Late Cenozoic shortening in the west-central Alborz Mountains, northern Iran, by combined conjugate strike-slip and thin-skinned deformation. *Geosphere*, 2(1), 35–52.
- Gutenberg, B., & Richter, C. F. (1944). Frequency of earthquakes in California. *Bulletin of the Seismological Society of America*, 34(4), 185–188.
- Hassani, B., Zafarani, H., Farjoodi, J., & Ansari, A. (2011). Estimation of site amplification, attenuation and source spectra of S-waves in the East-Central Iran. *Soil Dynamics and Earthquake Engineering*, 31(10), 1397–1413.
- Heimpel, M. (1997). Critical behaviour and the evolution of fault strength during earthquake cycles. *Nature*, 388(6645), 865–868.
- Herring, T. A., King, R. W., & McCully, S. C. (2010). *GLOBK reference manual, global Kalman filter VLBI and GPS analysis program, Release 10.4*, Department of Earth, Atmospheric, and Planetary Sciences, MIT.
- Hollingsworth, J., Nazari, H., Ritz, J.-F., Salamati, R., Talebian, M., & Bahroudi, A., et al. (2010). Active tectonics of the east Alborz mountains, NE Iran: Rupture of the left-lateral Astaneh fault system during the great 856 A.D. Qumis earthquake. *Journal of Geophysical Research*. doi:10.1029/2009JB007185, b12313.
- Hu, F., Zhang, Z., & Chen, X. (2016). Investigation of earthquake jump distance for strike-slip step overs based on 3D dynamic rupture simulations in an elastic half-space. *Journal of Geophysical Research*, 121(2), 994–1006. doi:10.1002/2015JB012696.
- Jackson, J., Haines, J., & Holt, W. (1995). The accommodation of Arabia-Eurasia plate convergence in Iran. *Journal of Geophysical Research*, 100, 15205–15219. doi:10.1029/95JB01294.
- Kamer, Y., & Hiemer, S. (2015). Data-driven spatial b value estimation with applications to California seismicity: To b or not to b. *Journal of Geophysical Research*, 120(7), 5191–5214.
- Kanamori, H., & Allen, C. R. (2013). *Earthquake Repeat Time and Average Stress Drop*. American Geophysical Union, pp. 227–235. doi:10.1029/GM037p0227.
- Kanamori, H., & Anderson, D. L. (1975). Theoretical basis of some empirical relations in seismology. *Bulletin of the Seismological Society of America*, 65(5), 1073–1095.
- Khodaverdian, A., Zafarani, H., & Rahimian, M. (2015). Long term fault slip rates, distributed deformation rates and forecast of seismicity in the Iranian Plateau. *Tectonics*, 34(10), 2190–2220.
- Knopoff, L., & Gardner, J. K. (1972). Higher seismic activity during local night on the raw worldwide earthquake catalogue. *Geophysical Journal of the Royal Astronomical Society*, 28(3), 311–313.
- Kondorskaya, N., & Shebalin, N. (2010). New catalog of strong earthquakes in the U.S.S.R. from ancient times through 1977, *Tech. rep.*, NOAA, National Geophysical Data Center, Boulder, Colorado, USA.
- Kostrov, B. V., & Das, S. (1988). *Principles of Earthquakes Source Mechanics*. Cambridge University Press, Cambridge, p. 286.
- Lay, T., & Wallace, T. (1995). *Modern Global Seismology*. International Geophysics. California, United States, Elsevier Science, p. 521.
- Lengliné, O., Lamourette, L., Vivin, L., Cuenot, N., & Schmittbuhl, J. (2014). Fluid-induced earthquakes with variable stress drop. *Journal of Geophysical Research*, 119(12), 8900–8913. doi:10.1002/2014JB011282.
- McGill, S. F., Spinler, J. C., McGill, J. D., Bennett, R. A., Floyd, M. A., Fryxell, J. E., et al. (2015). Kinematic modeling of fault slip rates using new geodetic velocities from a transect across the Pacific-North America plate boundary through the San Bernardino Mountains, California. *Journal of Geophysical Research*, 120(4), 2772–2793.
- Meade, B. J., & Hager, B. H. (2005). Block models of crustal motion in southern California constrained by GPS measurements. *Journal of Geophysical Research*, 110(B3), B03403.
- Masson, F., Chéry, J., Hatzfeld, D., Martinod, J., Vernant, P., Tavakoli, F., et al. (2005). Seismic versus aseismic deformation in Iran inferred from earthquakes and geodetic data. *Geophysical Journal International*, 160(1), 217–226.
- Mirzaei, N., Gao, M., & Chen, Y. (1997). Seismicity in major seismotectonic provinces of Iran. *Earthquake Research in China*, 11, 351–361.
- Mirzaei, N., Gao, M., & Chen, Y. (1999). Delineation of potential seismic sources for seismic zoning of Iran. *Journal of Seismology*, 3, 17–30.
- Mousavi, Z., Walpersdorf, A., Walker, R., Tavakoli, F., Pathier, E., Nankali, H., et al. (2013). Global Positioning System constraints on the active tectonics of NE Iran and the South Caspian region. *Earth and Planet. Science Letters*, 377, 287–298.
- Mullick, M., Riguzzi, F., & Mukhopadhyay, D. (2009). Estimates of motion and strain rates across active faults in the frontal part of eastern Himalayas in North Bengal from GPS measurements. *Terra Nova*, 21, 410–415.
- Nakamura, T., Suzuki, S., Sadeghi, H., Fatemi Aghda, S. M., Matsushima, T., Ito, Y., Hosseini, S. K., Gandomi, A. J., & Maleki, M. (2005). Source fault structure of the 2003 Bam earthquake, southeastern Iran, inferred from the aftershock distribution and its relation to the heavily damaged area: Existence of the Arg-e-Bam fault proposed. *Geophysical Research Letters*. doi:10.1029/2005GL022631.
- National Geophysical Data Center, NOAA (2016). National Geophysical Data Center / World Data Service (NGDC/WDS): Global Significant Earthquake Database. <http://www.ngdc.noaa.gov/nndc/struts/form?t=101650&s=1&d=1>. doi:10.7289/V5TD9V7K, online; Accessed Jan 2016.
- Nazari, H., Ritz, J.-F., Salamati, R., Shafei, A., Ghassemi, A., Michelot, J.-L., et al. (2009). Morphological and palaeoseismological analysis along the Taleghan fault (Central Alborz, Iran). *Geophysical Journal International*, 178(2), 1028–1041. doi:10.1111/j.1365-246X.2009.04173.x.
- Nilforoushan, F., Masson, F., Vernant, P., Vigny, C., Martinod, J., Abbassi, M., et al. (2003). GPS network monitors the Arabia-Eurasia collision deformation in Iran. *Journal of Geodesy*, 77(7–8), 411–422.

- Nissen, E., Jackson, J., Jahani, S., & Tatar, M. (2014). Zagros “phantom earthquakes” reassessed—The interplay of seismicity and deep salt flow in the Simply Folded Belt? *Journal of Geophysical Research*, *119*(4), 3561–3583.
- Nowroozi, A. A., & Ahmadi, G. (1986). Analysis of earthquake risk in Iran based on seismotectonic provinces. *Tectonophysics*, *122*, 89–114.
- Nur, A., & Mavko, G. (1974). Postseismic viscoelastic rebound. *Science*, *183*(4121), 204–206.
- Okal, E. A., & Romanowicz, B. A. (1994). On the variation of b-values with earthquake size. *Physics of the Earth and Planetary Interiors*, *87*(1–2), 55–76. doi:10.1016/0031-9201(94)90021-3.
- Ottmüller, L., Voss, P., & Havskov, J. (2013). *SEISAN earthquake analysis software for Windows*. Linux and MacOSX: Solaris.
- Riznichenko, Y. V. (1965). *Seismic rock flow, in dynamics of the Earth's crust*. Moscow: Nauka.
- Savage, J., & Prescott, W. (1978). Asthenosphere readjustment and the earthquake cycle. *Journal of Geophysical Research*, *83*(B7), 3369–3376.
- Scholz, C. H. (2015). On the stress dependence of the earthquake b value. *Geophysical Research Letters*, *42*(5), 1399–1402. doi:10.1002/2014GL062863.
- Schorlemmer, D., & Wiemer, S. (2005). Earth science: Micro-seismicity data forecast rupture area. *Nature*, *434*(7037), 1086–1086.
- Shabanian, E., Bellier, O., Siame, L., Abbassi, M. R., Bourlés, D., & Braucher, R., et al. (2012). The Binalud Mountains: A key piece for the geodynamic puzzle of NE Iran. *Tectonics*, *31*(6), doi:10.1029/2012TC003183, tC6003.
- Sorbi, M. R., Nilfouroushan, F., & Zamani, A. (2012). Seismicity patterns associated with the September 10th, 2008 Qeshm earthquake, South Iran. *International Journal of Earth Sciences*, *101*(8), 2215–2223.
- Sugan, M., Kato, A., Miyake, H., Nakagawa, S., & Vuan, A. (2014). The preparatory phase of the 2009 Mw 6.3 L'Aquila earthquake by improving the detection capability of low-magnitude foreshocks. *Geophysical Research Letters*, *41*(17), 6137–6144.
- Talebian, M., Fielding, E. J., Funning, G. J., Ghorashi, M., Jackson, J., & Nazari, H., et al. (2004). The 2003 Bam (Iran) earthquake: Rupture of a blind strike-slip fault. *Geophysical Research Letters*. doi:10.1029/2004GL020058.
- Tatar, M., & Hatzfeld, D. (2009). Microseismic evidence of slip partitioning for the Rudbar-Tarom earthquake (Ms 7.7) of 1990 June. *Geophysical Journal International*, *176*(2), 529–541.
- Tavakoli, B., & Ghafory Ashtiany, M. (1999). Seismic hazard assessment of Iran. *Annals of Geophysics*, *42*, 1013–1021.
- Tavakoli, F., Walpersdorf, A., Authemayou, C., Nankali, H., Hatzfeld, D., Tatar, M., et al. (2008). Distribution of the right-lateral strike-slip motion from the Main Recent Fault to the Kazerun Fault System (Zagros, Iran): Evidence from present-day GPS velocities. *Earth and Planetary Science Letters*, *275*(3–4), 342–347. doi:10.1016/j.epsl.2008.08.030.
- Unglert, K., Savage, M. K., Fournier, N., Ohkura, T., & Abe, Y. (2011). Shear wave splitting, v_p/v_s , and GPS during a time of enhanced activity at Aso caldera, Kyushu. *Journal of Geophysical Research*, *116*(B11). doi:10.1029/2011JB008520.
- Vallée, M. (2013). Source time function properties indicate a strain drop independent of earthquake depth and magnitude. *Nature Communications*, *4*, 2606.
- Walters, R., Parsons, B., & Wright, T. (2014). Constraining crustal velocity fields with InSAR for Eastern Turkey: Limits to the block-like behavior of Eastern Anatolia. *Journal of Geophysical Research*, *119*(6), 5215–5234.
- Walpersdorf, A., Manighetti, I., Mousavi, Z., Tavakoli, F., Vergnolle, M., Jadidi, A., et al. (2014). Present day kinematics and fault slip rates in eastern Iran derived from 11 years of GPS data. *Journal of Geophysical Research*, *119*, 1359–1383.
- Wiemer, S., & Schorlemmer, D. (2007). ALM: An asperity-based likelihood model for California. *Seismological Research Letters*, *78*(1), 134–140.
- Wiemer, S., & Wyss, M. (2002). Mapping spatial variability of the frequency-magnitude distribution of earthquakes. *Advances in Geophysics*, *45*, 259–302.
- Wyss, M., Liang, B., Tanigawa, W., & Wu, X. (1992). Comparison of orientations of stress and strain tensors based on fault plane solutions in Kaoiki, Hawaii. *Journal of Geophysical Research*, *97*(B4), 4769–4790.
- Wyss, M., Schorlemmer, D., & Wiemer, S. (2000). Mapping asperities by minima of local recurrence time: San Jacinto-Elsinore fault zones. *Journal of Geophysical Research*, *105*(B4), 7829–7844.
- Yamasaki, T., Wright, T. J., & Houseman, G. A. (2014). Weak ductile shear zone beneath a major strike-slip fault: Inferences from earthquake cycle model constrained by geodetic observations of the western North Anatolian Fault Zone. *Journal of Geophysical Research*, *119*(4), 3678–3699.
- Zafarani, H., & Hassani, B. (2013). Site response and source spectra of S waves in the Zagros region, Iran. *Journal of Seismology*, *17*(2), 645–666.
- Zafarani, H., Hassani, B., & Ansari, A. (2012). Estimation of earthquake parameters in the Alborz seismic zone, Iran using generalized inversion method. *Soil Dynamics and Earthquake Engineering*, *42*, 197–218.
- Zarifi, Z., Nilfouroushan, F., & Raeesi, M. (2014). Crustal stress map of Iran: Insight from seismic and geodetic computations. *Pure and Applied Geophysics*, *171*, 1219–1236. doi:10.1007/s00024-013-0711-9.
- Zielke, O., & Arrowsmith, J. (2008). Depth variation of coseismic stress drop explains bimodal earthquake magnitude-frequency distribution. *Geophysical Research Letters*, *35*(24), L24301.